

Review

# Recent Advances in Perovskite Catalysts for Efficient Overall Water Splitting

Conghui Si \*, Wenchao Zhang, Qifang Lu, Enyan Guo, Zhou Yang, Jiyun Chen, Xinya He and Jing Luo

Shandong Provincial Key Laboratory of Processing and Testing Technology of Glass & Functional Ceramics, School of Material Science and Engineering, Qilu University of Technology (Shandong Academy of Sciences), Jinan 250353, China; zhwc98@163.com (W.Z.); luqf0324@126.com (Q.L.); guoenyan1985@126.com (E.G.); yanglife8023@163.com (Z.Y.); chenjiyun7398@163.com (J.C.); hxinya0522@163.com (X.H.); luojing03162021@163.com (J.L.)

\* Correspondence: conghui\_si@qlu.edu.cn

**Abstract:** Hydrogen is considered a promising clean energy vector with the features of high energy capacity and zero-carbon emission. Water splitting is an environment-friendly and effective route for producing high-purity hydrogen, which contains two important half-cell reactions, namely, the anodic oxygen evolution reaction (OER) and the cathodic hydrogen evolution reaction (HER). At the heart of water splitting is high-performance electrocatalysts that efficiently improve the rate and selectivity of key chemical reactions. Recently, perovskite oxides have emerged as promising candidates for efficient water splitting electrocatalysts owing to their low cost, high electrochemical stability, and compositional and structural flexibility allowing for the achievement of high intrinsic electrocatalytic activity. In this review, we summarize the present research progress in the design, development, and application of perovskite oxides for electrocatalytic water splitting. The emphasis is on the innovative synthesis strategies and a deeper understanding of structure–activity relationships through a combination of systematic characterization and theoretical research. Finally, the main challenges and prospects for the further development of more efficient electrocatalysts based on perovskite oxides are proposed. It is expected to give guidance for the development of novel non-noble metal catalysts in electrochemical water splitting.

**Keywords:** perovskite oxides; electrocatalytic water splitting; oxygen evolution reaction (OER); hydrogen evolution reaction (HER); hydrogen



**Citation:** Si, C.; Zhang, W.; Lu, Q.; Guo, E.; Yang, Z.; Chen, J.; He, X.; Luo, J. Recent Advances in Perovskite Catalysts for Efficient Overall Water Splitting. *Catalysts* **2022**, *12*, 601. <https://doi.org/10.3390/catal12060601>

Academic Editor: Yurii V. Geletii

Received: 5 April 2022

Accepted: 26 May 2022

Published: 31 May 2022

**Publisher's Note:** MDPI stays neutral with regard to jurisdictional claims in published maps and institutional affiliations.



**Copyright:** © 2022 by the authors. Licensee MDPI, Basel, Switzerland. This article is an open access article distributed under the terms and conditions of the Creative Commons Attribution (CC BY) license (<https://creativecommons.org/licenses/by/4.0/>).

## 1. Introduction

With the depletion of fossil fuels and the increased concerns about environmental pollution, considerable efforts have been made to search for renewable and clean energy alternatives [1]. Hydrogen gas (H<sub>2</sub>) is a clean fuel that can be used without producing pollutants or greenhouse gas and possesses a high specific energy of 122 kJ/g [2]. Vehicles driven by hydrogen fuel cells can dramatically reduce the dependence on fossil fuels and significantly bring down exhaust emissions [3]. Generating hydrogen gas through non-renewable resources such as coal, oil, and natural gas is still dominant in the global industry. For example, about 95% of hydrogen gas is produced from fossil-fuels-dependent steam reforming [4,5].

In contrast, electrochemical water splitting is recognized as a highly promising technology for sustainably producing high purity hydrogen gas [6]. The electricity can be derived from intermittent energy sources, such as solar, tidal, and wind energy [7]. As shown in Figure 1a,b, the publication numbers of “water electrolysis” and “electrocatalytic water splitting” have increased significantly in the past 10 years. The oxygen evolution reaction (OER) at the anode and the hydrogen evolution reaction (HER) at the cathode are a pair of essential electrochemical reactions for overall electrochemical water splitting. However, due to the sluggish kinetics of OER and HER, large overpotentials are usually

required to drive water splitting. It is imperative to develop efficient electrocatalysts for OER and HER in order to dramatically reduce the overpotential and increase the efficiency. Precious metal-based catalysts such as  $\text{IrO}_2/\text{RuO}_2$  and  $\text{Pt}/\text{C}$  have been recognized as the state-of-the-art electrocatalysts for OER and HER, respectively, but they suffer from the shortcomings of scarcity, high cost, and poor stability [8]. These limitations have largely restricted the competitiveness of electrochemical water splitting, with less than 5% of global hydrogen gas being generated through this technique. Substantial efforts have been devoted to exploiting the high-performance, cost-effective, and abundant electrocatalysts for water splitting, including transition metal oxides, hydroxides, phosphides, chalcogenides, selenides, nitrides, carbides, etc. [9–14].

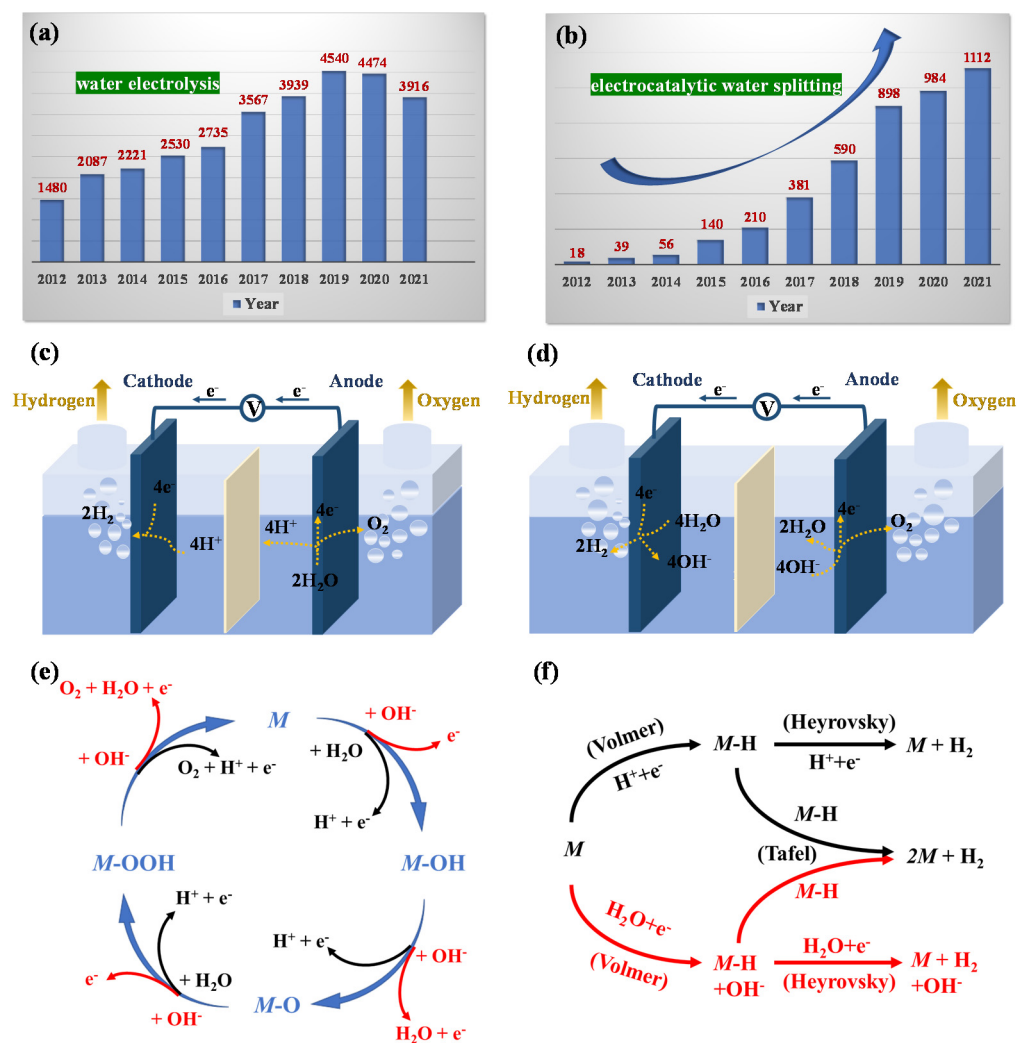


**Figure 1.** Roughly estimated numbers of publications during 2012–2021 from Web of Science, which were obtained by searching the following keywords: (a) “water electrolysis” and (b) “electrocatalytic water splitting”. Schematic illustration of an archetypal electrolysis cell for water splitting under (c) acidic conditions and (d) alkaline solutions. (e) The OER mechanism for acid (black line) and alkaline (red line) conditions. (f) The HER mechanism for acid (black line) and alkaline (red line) conditions.

Recently, perovskite oxides (i.e.,  $\text{ABO}_3$ , where A is the alkaline and/or rare earth metal and B is the transition metal) have emerged as promising catalysts for water splitting due to their structural and compositional flexibility, adjustable electronic structure, environmental friendliness, and chemical durability [15]. Until now, perovskite oxides have emerged as excellent OER electrocatalysts. However, their HER performance is still unsatisfactory due to the low intrinsic electrical conductivity and activity of most single-phase perovskite oxides, thus impeding the practical application of perovskite oxides in overall water splitting. Lots

of strategies, such as doping and defect engineering [16], surface modification [17], and morphological control [18], have been utilized to regulate the surface properties, crystal structure, and electronic structure of perovskite oxides, thus optimizing the electrocatalytic behavior. Specifically, the structure and chemical composition of perovskite oxides are highly tunable based on the specific catalytic reactions. Perovskite oxides with various chemical elements and different crystal structures can possibly be achieved through doping at the A-, B-, and/or O-site or through creating nonstoichiometry with a new formula of  $A_xA'_{1-x}B_yB'_{1-y}O_{3 \pm \delta}$ . Further, due to the electrocatalytic reactions usually taking place on the catalyst surface, their physicochemical properties can be altered through surface modification, such as surface reconstruction [19], exsolution [20], solvent-induced surface hydroxylation [21], and phosphate ion functionalization [22]. Thirdly, tailoring morphological structures is also a very effective way to improve the electrochemical surface area of the catalysts and thus the extrinsic activity. Last but not least, the internal electronic structure of perovskite oxides also strongly influences the OER/HER catalytic activity by modifying the surface lattice oxygen, the metal–oxygen covalency, the oxidation state of the B-site metals, the interaction between the B-site and O-site ions, the  $e_g$  orbital occupancy, the  $d$ -band center of the transition metal, and the  $p$ -band center of the oxygen relative to the Fermi level [23].

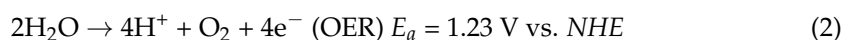
At present, the review articles regarding perovskite oxides for electrocatalysis have mainly focused on the following topics: perovskite oxides as oxygen electrocatalysts for oxygen reduction reaction (ORR) and OER, photoelectrochemical water splitting, double perovskites and derivatives, the nanostructuring methods of perovskite electrocatalysts, etc. [24–28]. However, only a few reviews reported the preparation, design, improvement, and application of the specific category of perovskite oxides in electrocatalytic water splitting. In this article, the recent development of perovskite oxides as OER/HER catalysts in electrochemical water splitting has been carefully reviewed, with subsections on the general mechanisms of water splitting, the superiority of perovskite oxides as electrocatalysts for water splitting, and the performance improvement strategies for electrocatalytic water splitting. The challenges in the synthesis of perovskites are also discussed.

## 2. General Mechanisms of Water Splitting

A deep understanding of the OER/HER mechanisms in water splitting is undoubtedly necessary to gain insights into issues such as how to determine the reaction rates and how to offer directions for the design and synthesis of electrocatalysts. As noted above, the overall water splitting mechanism consists of two half-reactions (i.e., OER at the anode and HER at the cathode) that take place simultaneously [29]. Typical water electrolysis cells under acidic conditions and alkaline solutions are shown in Figure 1c,d, respectively. Water splitting can proceed in a wide pH range via an overall reaction:



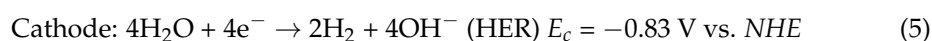
Under acidic conditions (pH = 0), the water is oxidized at the anode according to the following equation:



Electrons and protons are combined at the cathode to generate  $\text{H}_2$ :



Under alkaline conditions (pH = 14), the OER and HER processes proceed according to the equations below, respectively.

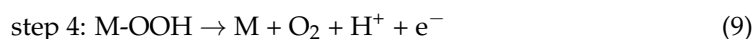
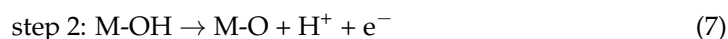
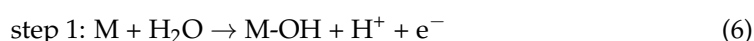


According to the Nernst Equations, the theoretical thermodynamic potential to drive water electrolysis is 1.23 V at 25 °C and 1 atm. However, overpotential has to be applied to make the reactions proceed at appreciable rates. The overpotential implies a potential bias above 1.23 V, which can be significant, resulting in the low efficiency of water electrolysis. Developing highly active water electrolysis catalysts with a low overpotential of OER and HER has been an efficacious strategy to address the challenges [30,31].

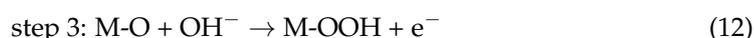
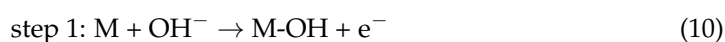
### 2.1. General OER Mechanism

OER is a relatively complex reaction involving multielectron/proton transfer that makes it more challenging to improve the overall reaction kinetics [32]. As shown in Figure 1e, the possible OER mechanism can be divided into four steps regardless of whether it is under acidic or alkaline conditions [33,34]:

Under acidic conditions:



Under alkaline conditions:



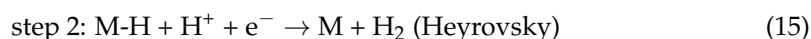
Typically, the oxidation of the  $H_2O/OH^-$  species is initiated to form M-OH (Equations (6) and (10)), followed by deprotonation and further oxidation to generate M-O (Equations (7) and (11)) and M-OOH (Equations (8) and (12)) intermediates and ultimately  $O_2$  products (Equations (9) and (13)) under the electrochemical oxidation condition. Under acidic conditions,  $H_2O$  molecules serve as the oxygen source, while under alkaline conditions, the oxygen is from  $OH^-$  ions.

The adsorption of these intermediates on the catalyst surface is a prerequisite for OER, and ideal OER catalysts should have optimal binding energies towards these intermediates. The multiple intermediates during OER pose difficulties for the rapid kinetics due to the accumulative energy barriers.

### 2.2. General HER Mechanism

Compared with OER, HER, with two electron transfer steps, occurs relatively easy (Figure 1f). The ‘Volmer–Heyrovsky’ and ‘Volmer–Tafel’ mechanisms have been widely accepted as the general mechanisms of HER [35,36]:

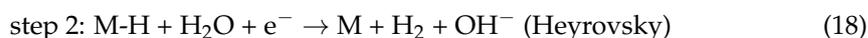
Under acidic conditions:



or



Under alkaline conditions:



or



The first step is the combination of  $\text{H}^+/\text{H}_2\text{O}$  and an electron on the catalyst surface, which results in an adsorbed hydrogen atom (also called the Volmer step, Equations (14) and (17)). After producing an adsorbed hydrogen atom, there are two possible steps: combine  $\text{H}^+/\text{H}_2\text{O}$  and an electron (Heyrovsky step, Equations (15) and (18)) or another adsorbed hydrogen atom (Tafel step, Equations (16) and (19)) to produce a hydrogen molecule. The Volmer–Heyrovsky steps occur preferentially when the coverage of the adsorbed hydrogen on the catalyst surface is relatively low. On the contrary, the faster Volmer–Tafel steps take place under a high adsorbed hydrogen coverage.

### 2.3. OER/HER Mechanisms for Perovskite Oxides

Understanding the OER/HER mechanisms occurring on the perovskite oxide surfaces is of particular importance for the optimization of the catalyst performances. The process of OER is complicated, with multiple steps, and the reaction pathways can vary depending on the different catalysts utilized as well. Conventionally, the adsorbate evolution mechanism (AEM) is proposed to explain the OER reaction pathway occurring on perovskite oxides in alkaline solutions [37] (Figure 2a). The AEM typically involves four consecutive proton-coupled electron transfers (PCET) occurring solely on the B-site metal ion center. Recent studies indicated that the lattice-oxygen participation mechanism (LOM) can take place simultaneously in the OER process [38] (Figure 2b). This mechanism involves the participation of lattice oxygen, which signifies that the surface metal atom is not the only active center. Indeed, if only the AEM is assumed to occur, the optimization of the adsorption–desorption strength for the surface transition metal ions that participate in bonding with the surface adsorbates is the key strategy to improve the catalytic performance of OER. In AEM, the  $e_g$  occupancy of the surface transition metal ions and adsorbates is usually used as a descriptor to evaluate the OER activity of catalysts [39]. However, if the LOM also plays a role in the overall OER mechanism, the formation of lattice oxygen bypasses the formation of the  $\text{OOH}_{\text{ads}}$  intermediate, which significantly promotes the OER activity. The strengthening of the metal–oxygen covalency is an effective strategy to tailor the electronic structure of the catalysts and switch the OER pathway from the AEM to the LOM, which could be realized by defect engineering and elemental doping.

The probable HER mechanism for perovskite oxides in an alkaline medium is also shown in Figure 2c. In this mechanism, the HER reactive site for perovskite oxides is not metal but rather the negatively charged surface oxygen [40]. In the first step, the  $\text{H}_2\text{O}$  molecule from the electrolyte interacts with a connecting oxygen site to form an intermediate of adsorbed H; meanwhile, the adjacent metal site gets oxidized or reduced. In the second step, it is hard to say whether this step proceeds via the Tafel reaction or the Heyrovsky reaction. The reaction rate of HER is a strong function of the binding potential of the adsorbed H intermediate, which is generally referred to as hydrogen adsorption free energy ( $\Delta G_{\text{H}}$ ) [41]. An ideal HER catalyst has a moderate ability to bind hydrogen, providing a  $\Delta G_{\text{H}}$  value of nearly zero (e.g., Pt).

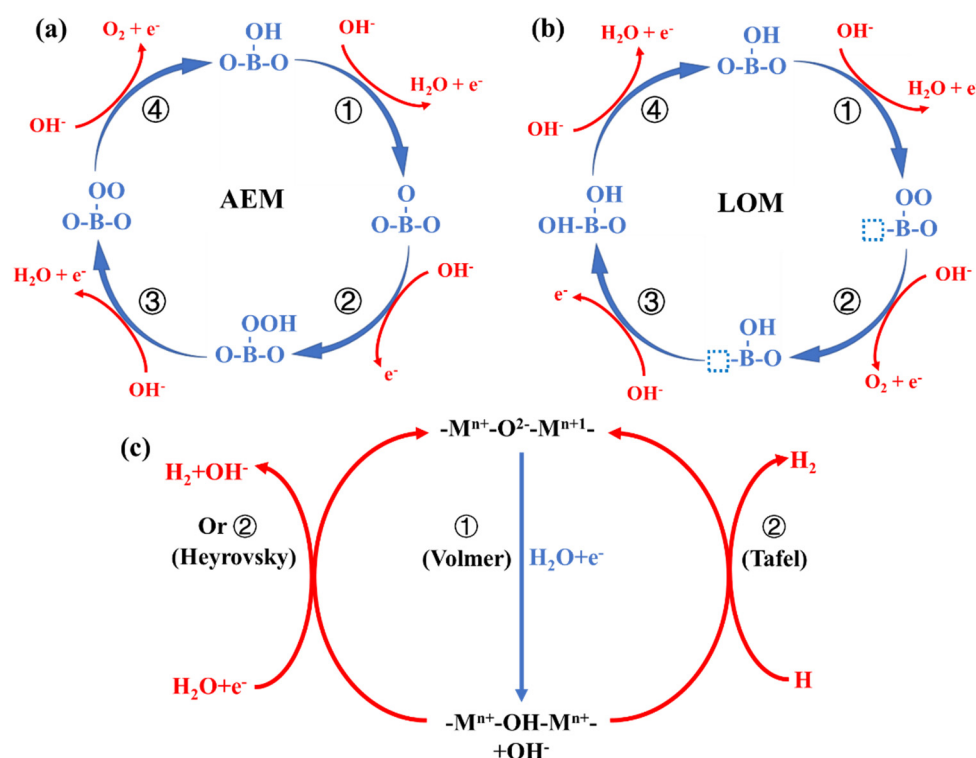


**Figure 2.** Proposed OER/HER mechanism on perovskite oxide catalysts. (a) The adsorbate evolution mechanism (AEM) for the OER on perovskite surfaces in alkaline solutions. (b) The lattice-oxygen participation mechanism (LOM) for the OER on perovskite surfaces in alkaline solutions. (c) Mechanism for HER on the surface of perovskite oxides in alkaline solutions.

### 3. The Key Aspects of Perovskite Oxides as Electrocatalysts for Water Splitting

Based on the general mechanisms of electrochemical water splitting discussed above, the ideal electrocatalysts should possess a series of advantages, including: (i) a composition with inexpensive earth-abundant material, (ii) improved intrinsic activity and long-term stability, and (iii) an efficient large-scale synthesis strategy.

#### 3.1. Structural and Compositional Flexibility

A major superiority of perovskite oxides is the structural and compositional flexibility for tuning their physical, chemical, and catalytic properties. As shown in Figure 3a, in an ideal cubic cell without oxygen vacancies, the perovskite oxide ( $\text{ABO}_3$ ) has a high symmetry of Pmm3 comprised of a highly flexible framework built up from chains of corner-sharing  $[\text{BO}_6]$  octahedra, with the larger A-site occupying the 12-fold coordinated sites within the cavity of eight octahedra. More than 90% of metal elements within the “Periodic Table of Elements” can form perovskite-type oxides by doping/substituting elements at the A- or/and B-site [42]. Figure 3b highlights the elements that have appeared on the A- or B-site in perovskite oxides available in the experimental data. Additionally, the oxygen nonstoichiometry value can also vary over a wide range. Due to the diversity of the constituent elements, a variety of perovskite oxides can be obtained with the formula  $\text{A}_x\text{A}'_{1-x}\text{B}_y\text{B}'_{1-y}\text{O}_{3\pm\delta}$ . Moreover, a variety of perovskite derivatives are added to the perovskite family, such as the double perovskite [43], layered perovskite [44], quadruple perovskite [45], and so on. The great flexibility of the composition and crystal structure gives rise to the tunable electronic structure of perovskite oxides and their diverse physico-chemical properties [8].

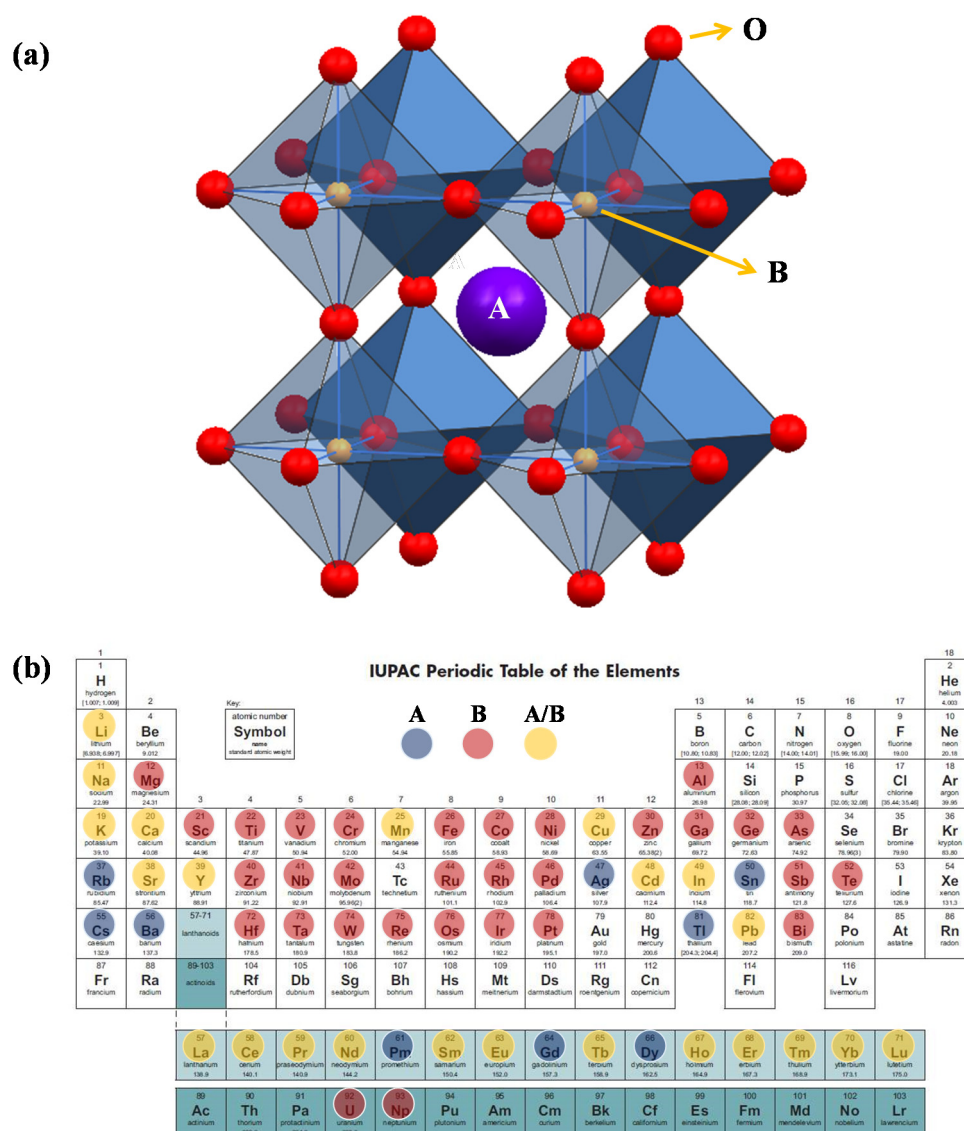


**Figure 3.** (a) Schematic illustration of an ideal perovskite oxide unit cell. (b) The elements that appeared on the A- or B-site in perovskite oxides available in the experimental data. The blue label represents the A-site, the red label represents the B-site, and the yellow label represents either the A- or B-site.

### 3.1.1. Structural Flexibility

In addition to single perovskites, double perovskites have attracted widespread interest in recent years. In the double perovskites, the A- or B-site is occupied by two different types of cations, giving the formulas of AA'B<sub>2</sub>O<sub>6</sub> (double A-site) or A<sub>2</sub>BB'O<sub>6</sub> (double B-site). Even though A' and A (B' and B) are sufficiently different in size and/or charge, the ordering of the A-site (or B-site) cation could also occur (Figure 4a) [25]. In general, the vast majority of double perovskites refer to A<sub>2</sub>BB'O<sub>6</sub> due to the physicochemical properties of perovskites being highly dependent on the B-site cations, while the A-site cations usually act as the electron donor to the [BO<sub>6</sub>] framework. Firstly, the double perovskites can accommodate elements that are not present in the single perovskites (e.g., high-valence elements such as 6<sup>+</sup> or 7<sup>+</sup>) [46]. Secondly, the atomic environment of double perovskites is more complex than that of single perovskites, resulting in an uncommon electronic structure. Thirdly, the stabilities of double perovskites under electrocatalytic conditions are obviously improved. Therefore, constructing the double perovskite structure is highly efficient for improving the catalytic performance for OER and HER. For instance, Sun et al. prepared double perovskite Sr<sub>2</sub>Fe<sub>0.8</sub>Co<sub>0.2</sub>Mo<sub>0.6</sub>Co<sub>0.4</sub>O<sub>6-δ</sub>

through smart composition control, which exhibits significantly enhanced OER activity in alkaline media, requiring an overpotential of 345 mV to reach a  $10 \text{ mA cm}^{-2}$  and a cell voltage of 1.57 V to afford the same current density for the overall water splitting when coupled with a Pt/C cathode [47]. Emerging as a family of outstanding alternatives in perovskites, layered perovskites have attracted considerable attention because of their high oxygen ionic-transport property [48]. With the formula  $A_2BO_{4+\delta}$ , layered perovskite oxides can be described as a stacked cubic perovskite ( $ABO_3$ ) layer alternating with a rock-salt (AO) layer along the *c* direction (Figure 4b) [49,50]. Due to the difference in the A-O and B-O bond lengths, there is stress in the  $A_2BO_{4+\delta}$  structure. To eliminate this stress and maintain structural stability, a lot of interstitial oxygen is present in the  $ABO_3$  layers and the AO layers, leading to fast oxygen transport, which is conducive to accelerating electrocatalytic reaction. For instance, Jung et al. reported a layered perovskite  $\text{La}_2\text{NiO}_4$  with high ORR and OER activities [50]. Rechargeable lithium-air and zinc-air batteries assembled with these catalysts exhibit remarkably reduced discharge-charge voltage gaps (improved round-trip efficiency) as well as high stability during cycling.

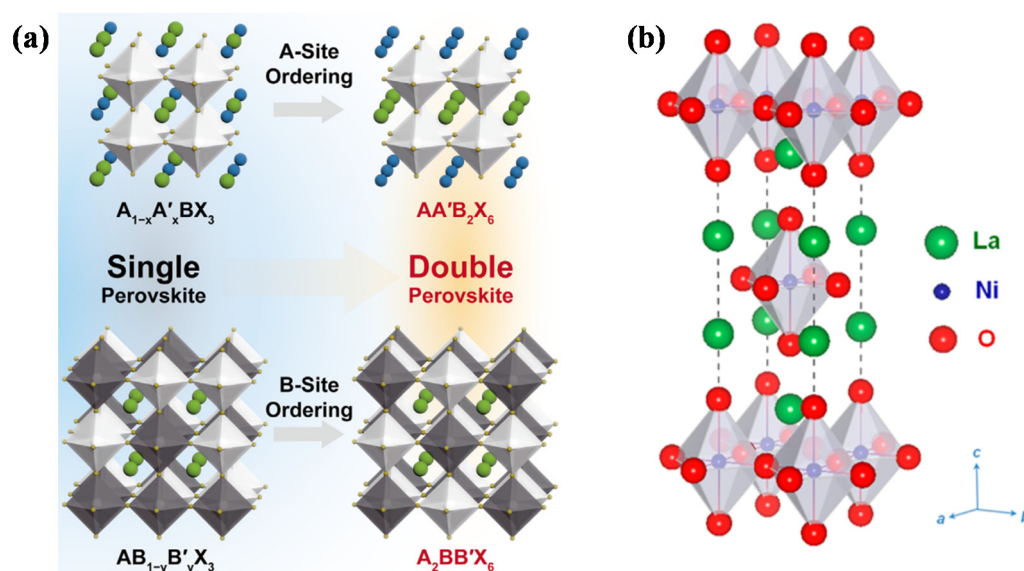


**Figure 4.** (a) Single perovskite (left) and double perovskite (right) with the A-site or B-site ordering. Reproduced with permission from ref. [25], Copyright 2019, Elsevier. (b) Crystal structure of  $\text{La}_2\text{NiO}_4$  layered perovskite. Reproduced with permission from ref. [50], Copyright 2013, American Chemical Society.

### 3.1.2. Compositional Flexibility

The substitution of elements at the A-, B-, and/or O-site and the introduction of oxygen ion vacancies have large characteristic effects on the electronic structure and coordination chemistry [51]. As a result, the OER/HER electrocatalytic performances of perovskites are closely associated with measurable parameters, including the  $e_g$  electron ( $\sigma^*$  orbital occupation), the B-O bond strength, the spin state, the *d*-band center of the transition metal, and the *p*-band center of the oxygen relative to the Fermi level (Figure 5) [52].

The B-sites of the perovskite oxides are usually served as the active sites and have an evident impact on their electrocatalytic activities. Improving the electrocatalytic properties of perovskites can be achieved by doping/substituting the B transition metal ion. Transforming the valence state of B-site cations is conducive for the formation of B-OH and the transmission of electron/oxygen [53]. Further, B-site doping may cause synergistic effects among the mixed metal cations, which are responsible for the electrocatalytic performance [54]. Recently, Wang et al. reported a new type of perovskite oxide-halide solid solution which had highly mixed elements and valences, uniform element distributions,

and single-phase crystalline structures. (Figure 6a–c) [55]. The perovskite oxide-halide solid solutions exhibit enhanced catalytic performance in the oxygen evolution reaction.

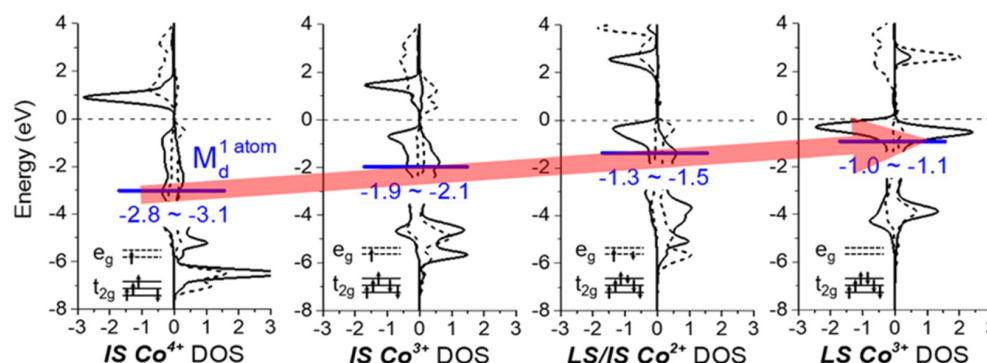


**Figure 5.** From left to right, intermediate spin states (IS) of  $\text{Co}^{4+}$ , IS of  $\text{Co}^{3+}$ , a crossover of  $\text{Co}^{2+}$  between intermediate- and low-spin states (IS/LS), and LS of  $\text{Co}^{3+}$ . Positive values indicate majority spin states, while negative values indicate minority spin states. The black dashed line represents the  $e_g$  orbital, and the solid black line represents the  $t_{2g}$  orbital of the Co 3d orbital. The solid blue line indicates the calculated d-band center ( $M_d$ ) position. The dashed horizontal line appears at the Fermi level, with occupied states at negative energies and unoccupied states at positive energies. Reproduced with permission from ref. [52], Copyright 2020, American Chemical Society.

Different from B-site cations, A-site cations have no effect on the electronic structure near the Fermi level, so they usually do not function as the active sites in the perovskite oxides but still play an important role in tailoring the valence state of B-site ions and thus tuning the strength of the B–O bond for OER and HER [56,57]. For instance, Wang et al. demonstrated a set of A-site substituted  $\text{RNiO}_3$  ( $R = \text{La}, \text{La}_{0.5}\text{Nd}_{0.5}, \text{La}_{0.2}\text{Nd}_{0.8}, \text{Nd}, \text{and } \text{Nd}_{0.5}\text{Sm}_{0.5}$ ) perovskite oxides as OER/ORR electrocatalysts and found that the OER activity initially increases upon substituting La with Nd and is maximal at  $\text{La}_{0.2}\text{Nd}_{0.8}\text{NiO}_3$  [56]. Recently, Li et al. reviewed the latest advances of A-site perovskite oxides as an emerging functional material in electrocatalysis and photocatalysis. In particular, the performance of A-site perovskite oxides (bimetallic, ternary metal, multimetallic, and oxynitride) in electrocatalysis and photocatalysis was systematically discussed in this review article (Figure 6d) [58].

Furthermore, due to the A–O bond being longer than the B–O bond, the A-site cations in the  $\text{ABO}_3$  framework can be selectively removed under special treatment conditions (i.e., acid solution), thus improving the electrocatalytic performance of perovskites. This strategy has been previously adopted for CO oxidation [59] and  $\text{NO}_x$  reduction [60] and has recently been extended into the electrocatalysts for OER/HER. For instance, Seitz et al. reported an  $\text{IrO}_x/\text{SrIrO}_3$  catalyst formed during electrochemical testing by Sr leaching from the surface layers of  $\text{SrIrO}_3$  thin films, which is highly active and stable for OER, with only 270 to 290 millivolts of overpotential for 30 h of continuous testing in acidic electrolytes, and substantially outperforms known  $\text{IrO}_x$  catalysts [61]. Although the exact structure of the surface formed during the reaction is still unknown, DFT calculations have identified possible structures that could be kinetically or epitaxially stabilized by the interface with  $\text{SrIrO}_3$  and could contribute to the very high observed activity. Similarly, Zhang et al. recently prepared a perovskite/spinel heterostructure, V-LCO/ $\text{Co}_3\text{O}_4$  (V-LCO refers to  $\text{LaCoO}_3$  with La and Co vacancies), through a double-cation gradient etching technique (Figure 7a) [19]. The V-LCO/ $\text{Co}_3\text{O}_4$  demonstrated significantly enhanced activity for OER, with an overpotential of 354 mV at  $10 \text{ mA cm}^{-2}$ , due to the heterogeneous interface effect and abundant vacancies (Figure 7b). Furthermore, the DFT calculation unveiled that the accelerated kinetics rate and superior catalytic activity are endowed by the suitable d-band center and the moderate adsorption strength for the OH species (Figure 7c,d).

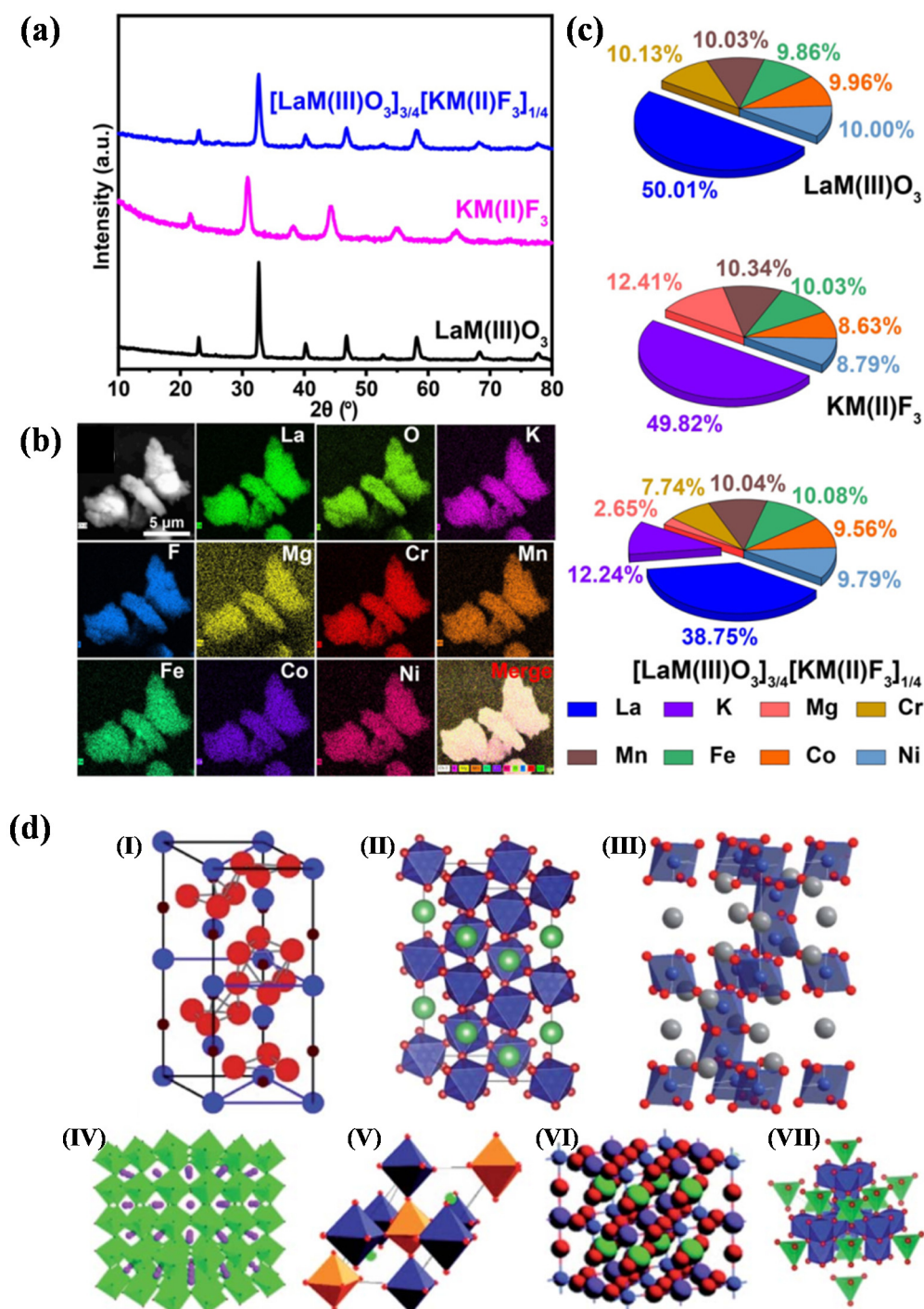


**Figure 6.** (a) XRD diffraction patterns of  $\text{LaM(III)}\text{O}_3$ ,  $\text{KM(II)}\text{F}_3$ , and  $[\text{LaM(III)}\text{O}_3]_{3/4}[\text{KM(II)}\text{F}_3]_{1/4}$ . (b) SEM EDX elemental mappings of La, O, K, F, Mg, Cr, Mn, Fe, Co, and Ni for  $\text{K(MgMnFeCoNi)}\text{F}_3$ . (c) Metal compositions (molar ratio) of  $\text{LaM(III)}\text{O}_3$ ,  $\text{KM(II)}\text{F}_3$ , and  $[\text{LaM(III)}\text{O}_3]_{3/4}[\text{KM(II)}\text{F}_3]_{1/4}$  calculated from the ICP-AES results. Reproduced with permission from ref. [55], Copyright 2021, Wiley. (d) Crystal structures of different A-site perovskite oxides: (I) structure of the rhombohedral cell in perovskite-type  $\text{BiFeO}_3$ ; (II) schematic illustration of the rhombohedral structured  $\text{LaCoO}_3$  perovskite; (III) hexagonal  $\text{BaTiO}_3$ ; (IV) crystal structure of porous  $\text{CaMnO}_3$ ; (V) orthorhombic structure; (VI) unit-cell polyhedral structure of  $\text{BaBi}_{0.1}\text{Sc}_{0.2}\text{Co}_{1.7}\text{O}_{6-x}$  at room temperature; (VII) crystal structure with  $\text{CuO}_4$  tetrahedra and  $\text{CoO}_6$  octahedra. Reproduced with permission from ref. [58], Copyright 2021, Royal Society of Chemistry.

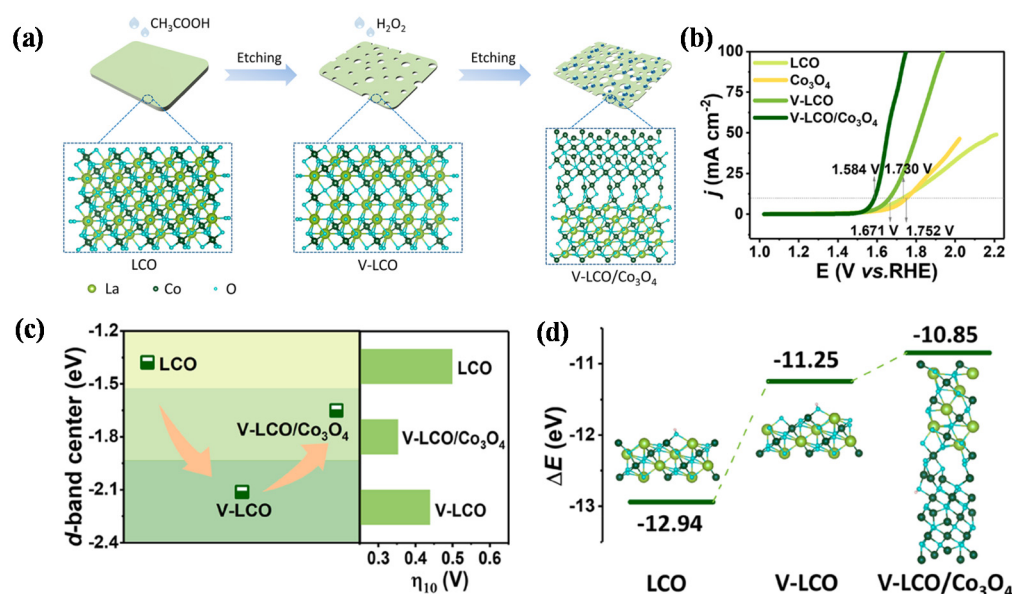


**Figure 7.** (a) Preparation process for the V-LCO/Co<sub>3</sub>O<sub>4</sub> heterostructure. (b) Polarization curves of LCO, V-LCO, V-LCO/Co<sub>3</sub>O<sub>4</sub>, and pure Co<sub>3</sub>O<sub>4</sub> for OER in 1.0 M KOH. (c) A comparison of the overpotential and the Co *d*-band centers of LCO, V-LCO, and V-LCO/Co<sub>3</sub>O<sub>4</sub>. (d) The surface adsorption energy difference ( $\Delta E$ ) for the OH of pristine LCO, V-LCO, and V-LCO/Co<sub>3</sub>O<sub>4</sub>. Reproduced with permission from ref. [19], Copyright 2021, American Chemical Society.

Traditionally, the transition metal ions are considered as active sites in the perovskites to catalyze the electrochemical surface reactions [62]. Recently, using the in situ <sup>18</sup>O isotope labeling mass spectrometry, Grimaud et al. provided direct experimental evidence of O<sub>2</sub> generated during the OER process on some highly active oxides that can come from lattice oxygen [63]. They also showed that increasing the covalency of metal–oxygen bonds is critical to triggering lattice oxygen oxidation and enabling non-concerted proton–electron transfers during OER. More and more studies indicated that the O-site in perovskites plays an important role in catalyzing OER and/or HER for water splitting [8,64]. The oxygen vacancies could be introduced into transition metal oxides by various techniques, such as thermal decomposition [65], the quenching approach [66], and post-annealing [67]. They greatly influence the electronic structure, transport properties, and absorption/desorption processes of the reactant and intermediates. The lattice oxygen could also be obtained by exchanging lattice oxygen species, and this process is strongly related to the oxygen vacancies. For instance, Bu et al. reported a new catalyst, P-3G, consisting of a cation-ordered perovskite (PrBa<sub>0.5</sub>Sr<sub>0.5</sub>)<sub>0.95</sub>Co<sub>1.5</sub>Fe<sub>0.5</sub>O<sub>5+ $\delta$</sub>  and 3D porous N-doped graphene, which exhibits outstanding multi-functional catalytic activities and excellent stabilities for OER and HER [68]. The water-splitting device using P-3G efficiently produced H<sub>2</sub> and O<sub>2</sub> gases at rates of 0.859  $\mu\text{L s}^{-1}$  and 0.417  $\mu\text{L s}^{-1}$ , respectively. They proposed that the improved OER activity is attributed to the increased covalency between the transition metals and lattice oxygen. Furthermore, the negative  $\Delta G_H$  on the lattice oxygen and the increased bond length (H\*–O) between H\* and the lattice oxygen enhance the HER activity.

### 3.2. Varied Synthesis Strategy

The microstructure, morphology, physicochemical property, specific surface area, and transport property of perovskite oxides are closely related to the synthesis strategy and further influence the electrocatalytic activity. Recently, several approaches have been developed to synthesize perovskite oxides, including conventional synthetic methods (i.e., the solid-state method, combustion synthesis, and high-pressure synthesis) [69,70], wet chemistry methods (i.e., the sol-gel process, co-precipitation method, and hydrothermal synthesis) [71–73], deposition approaches (i.e., physical vapor deposition, chemical va-

por deposition, and electrodeposition) [74–76], electrospinning [77], the polymer-assisted approach [78], and so on.

Among these methods, the conventional synthetic methods usually require a high reaction temperature and harsh reaction conditions such as high pressure and a special apparatus, leading to the formation of coarse perovskite particles with low specific surface areas ( $\sim 1\text{--}2\text{ m}^2\text{ g}^{-1}$ ) and porosity. The sol-gel process is often used to prepare perovskite-type composite oxides because this method may provide a high purity phase structure, a precise control of the composition, and the reduced temperature required for material synthesis. The co-precipitation method could also be used to synthesize well-defined perovskites such as  $\text{Sr}_2\text{M}(\text{IrO}_6)$  ( $\text{M} = \text{Fe}, \text{Co}$ ), which is explored as an excellent OER catalyst in acidic media [72]. Hydrothermal synthesis acts as one of the most attractive techniques for fabricating perovskites with various morphologies such as nanosheets [79], rod-like perovskites [80], nanoflakes [81], cubic perovskites [82], and nanoparticles [83]. However, the formation of perovskite oxides from hydrothermal synthesis usually involves subsequent annealing treatment, which requires a relatively high temperature.

In recent years, more and more attention has been paid to the preparation of perovskite oxides by deposition-based approaches. Physical vapor deposition (PVD) is a physical process including sputtering, laser ablation, and evaporation which has often been used to fabricate nanofilms. For instance, Risch et al. employed pulsed laser deposition to fabricate well-defined surfaces composed of  $\text{Ba}_{0.5}\text{Sr}_{0.5}\text{Co}_{0.8}\text{Fe}_{0.2}\text{O}_{3-\delta}$  on thin-film  $\text{La}_{0.8}\text{Sr}_{0.2}\text{MnO}_{3-\delta}$  grown on (001)-oriented Nb-doped  $\text{SrTiO}_3$  (BSCF | LSMO | NSTO), which comprise a two-component surface with bifunctionality for oxygen electrocatalysis [84]. The combined overpotentials from both OER and ORR kinetics on BSCF | LSMO | NSTO can be as low as 0.7 V, which rivals the intrinsic activities of the state-of-the-art catalysts in the literature. The chemical vapor deposition (CVD) method is more versatile in the control of the film composition and has been applied for the growth of various functional oxide materials, including perovskite oxides. For instance, Murauskas et al. prepared undoped  $\text{BaSnO}_3$  and La-doped  $\text{BaSnO}_3$  thin films through low-pressure pulsed injection liquid CVD modification (PI-MOCVD) based on the flash evaporation principle and precise precursor dosing into the reactor, providing easier control of the thin-film composition [75]. Electrodeposition is an electrochemical process that could precisely control the nucleation and growth of reactants as well as the structure, morphology, and purity of the target deposits. This method is a versatile synthetic approach to preparing abundant sediments on different substrates that only requires simple equipment. As a consequence, various morphologies such as  $\text{LaMnO}_3/\text{MnO}$  nano-arrays [85], nanoporous  $\text{LaFeO}_3$  [86], and  $\text{LaCo}_{0.8}\text{Fe}_{0.2}\text{O}_3$  nanoparticles [87] could be obtained through this approach.

Electrospinning is a simple, low-cost, and versatile technique for fabricating 1D nanostructure (e.g., nanofibers [88], nanotubes [89], and nanorods [8,90]) perovskite oxides. For example, Bian et al. prepared Mg-doped perovskite  $\text{LaNiO}_3$  nanofibers by the electrospinning method combined with subsequent calcination, which exhibit durable bifunctional OER/ORR electrocatalytic activity, with a lower overpotential of 0.45 V at a current density of  $10\text{ mA cm}^{-2}$  and a more positive half-wave potential of 0.69 V compared to those of the pristine  $\text{LaNiO}_3$  nanofibers [88]. The polymer-assisted method has recently been proven to be one of the most suitable processes to produce high-quality epitaxial complexes and multilayer-structured films in a very thin range below 100 nm. For instance, Wang et al. prepared double perovskite  $\text{La}_2\text{CoMnO}_6$  and  $\text{La}_2\text{NiMnO}_6$  epitaxial thin films through polymer-assisted deposition and subsequent crystallization by rapid thermal annealing. In addition to the above methods, our research group recently reported a new design concept and synthesis protocol for the direct transformation of bulk alloys into the nanoporous lanthanum-based perovskite oxide  $\text{LaMO}_3$  ( $\text{M} = \text{Co}, \text{Mn}, \text{Ni}, \text{or Cr}$ ) via a facile dealloying strategy [91]. The obtained  $\text{LaMO}_3$  perovskites display ultrahigh specific surface areas, exceptionally high ORR and OER activities, methanol resistance, and high operational durability under alkaline conditions.

## 4. Performance Improvement Strategies of Perovskite Oxides for Electrocatalytic Water Splitting

### 4.1. Doping/Substituting and Defect Engineering

#### 4.1.1. Doping/Substituting

The flexible perovskite structure allows for the incorporation of numerous dopants, and the electrocatalytic performances of perovskites are strongly dependent on their property, valence state, and doping position. The selective and functional doping/substituting in the A-, B-, and/or O-site of perovskite oxides is an effective strategy to obtain high OER/HER performance for water splitting.

As mentioned above, the A-site cations of perovskite oxides play a vital role in electrocatalytic activities. Firstly, the different cation radii and electronegativity of A-sites would lead to a change in the crystal structure, which results in different electronic properties. A-site cations can affect redox properties by adjusting the B-O interaction. For instance, Dai et al. synthesized a series of  $A\text{FeO}_3$  ( $A = \text{La}, \text{Nd}, \text{Eu}$ ) perovskite oxides [92]. This work confirmed that the Fe-O bond strength is related to the catalytic performance and the chemical structure of  $A\text{FeO}_3$ . The interplanar distance enlarges with the increase in the  $A^{3+}$  ionic radii ( $\text{La} = 1.36 \text{ \AA}$ ,  $\text{Nd} = 1.27 \text{ \AA}$ , and  $\text{Eu} = 1.21 \text{ \AA}$ ), increasing the Fe-O bond distance, which is related to the electronic structure of A-site cations. Therefore, the Fe-O bond is slightly longer in  $\text{LaFeO}_3$  than that in  $\text{NdFeO}_3$  and  $\text{EuFeO}_3$ . Secondly, the electronic conductivity can also be affected by A-site cations, because the  $4f$  electrons of the A-site cations contribute to the density of the states around the Fermi level. Thirdly, the appropriate doping/substituting of A-site cations will directly cause an increase in the oxygen vacancy and the optimization of the  $e_g$  occupation of B-site cations, resulting in the expansion of the lattice, which greatly improves the OER electrocatalytic activity. Finally, the valence state of B-site cations and the vacancy concentration of the O anion are also closely related to the adjustment of A-site stoichiometry.

Among the perovskite oxides,  $\text{Ba}_{0.5}\text{Sr}_{0.5}\text{Co}_{0.8}\text{Fe}_{0.2}\text{O}_{3-\delta}$  (BSCF) is one of the most attractive compounds; it exhibits extremely high OER/HER activities due to its optimal  $e_g$  orbital filling [93]. By modifying its surface electronic structures and properties through simple A-site doping, a highly efficient OER/HER electrocatalyst that is both active and stable in basic electrolytes could be obtained. For example, the Pr-doped BSCFs, such as  $\text{Pr}_{0.5}(\text{Ba}_{0.5}\text{Sr}_{0.5})_{0.5}\text{Co}_{0.8}\text{Fe}_{0.2}\text{O}_{3-\delta}$  ( $\text{Pr}_{0.5}\text{BSCF}$ ), exhibit significantly improved HER catalytic performance and durability compared to BSCF [57]. Nevertheless, surface amorphous phases in Pr-doped BSCF are still found after the durability test. It is reported that a smaller size mismatch between the host and dopant cations in the A-sites has a remarkable effect on rationalizing the stabilities and activities of cubic BSCF. For example, Hua et al. presented excellent catalytic performance and stability toward overall water splitting via La/Ca co-doping into the A-site of BSCF to form  $\text{La}_{0.5}(\text{Ba}_{0.4}\text{Sr}_{0.4}\text{Ca}_{0.2})_{0.5}\text{Co}_{0.8}\text{Fe}_{0.2}\text{O}_{3-\delta}$  (L-0.5) perovskite oxides [90]. The operating voltage of the integrated L-0.5/rGO electrolyzer is tested to be 1.76 V at  $50 \text{ mA cm}^{-2}$ , which is close to that of the commercially available  $\text{IrO}_2/\text{C-Pt}/\text{C}$  couple (1.76 V @  $50 \text{ mA cm}^{-2}$ ) Specifically, small amounts of Ca-doping can bring a significant increase in the corrosion resistance of perovskite oxides because  $\text{Ca}(\text{OH})_2$  and  $\text{CaCO}_3$  are easier to decompose than Ba (Sr) compounds.

In the bulk perovskite  $\text{ABO}_3$  structure, the  $d$ -orbital of the B-site transition metal and the  $p$ -orbital of the O-site would be hybridized or mixed to form  $\sigma$  and  $\pi$  orbitals (Figure 8a). The  $\sigma$  and  $\pi$  antibonding ( $\sigma^*$  and  $\pi^*$ ) orbitals are known as the  $e_g$  and  $t_{2g}$  orbitals in perovskites, respectively, with the  $\sigma^*$  orbital being more destabilized, or higher, in terms of energy. At the surface layer, the exposed B-sites have the coordination environment  $\text{BO}_5$ , with the apical (vertical) oxygen removed (Figure 8b). The  $e_g$  orbitals of the active B-site transition metal ions in the  $\text{BO}_5$  coordination capture surface-adsorbate bonding well, and the filling of the  $e_g$ -like states depends on the number of  $d$ -electrons and the spin state of the transition metal ions. The  $e_g$  occupancy approximates the strength of the adsorbate binding to the surface, with decreased  $e_g$  filling corresponding to increased adsorbate binding. For OER, the intrinsic activity of perovskites exhibits a volcano-shaped dependence on

the occupancy of the  $3d$ -electron with an  $e_g$  symmetry of the surface transition metal cations [93]. Therefore, it is important to develop a perovskite oxide with a surface cation with an  $e_g$  occupancy close to unity and high B-site oxygen covalency for enhancing the OER catalytic activity. As mentioned above, many investigations indicated that the BSCF perovskites with an optimal  $e_g \approx 1.2$  display a landmark intrinsic OER activity, which is at least an order of magnitude higher than the state-of-the-art  $\text{IrO}_2$  catalyst [93–95], while the deteriorated stability due to the surface amorphization during the OER process remains a serious challenge [96]. Recently, the modified hexagonal  $\text{Ba}_4\text{Sr}_4(\text{Co}_{0.8}\text{Fe}_{0.2})_4\text{O}_{15}$  (hex BSCF) perovskite with Co/Fe ions occupying two different tetrahedral and octahedral sites (Figure 8c) shows a remarkable OER activity, an extremely low overpotential of only 340 mV (and a small Tafel slope of  $47 \text{ mV dec}^{-1}$ ) in 0.1 M KOH, and excellent durability (Figure 8d,e) [97]. The O  $2p$ -band center has also been regarded as an effective descriptor for the OER catalytic activity of oxides. As seen from Figure 8f, the O  $2p$ -band center of hex BSCF is much higher than that of the pristine  $\text{Sr}_8\text{Co}_4\text{O}_{15}$ ,  $\text{Ba}_8\text{Co}_4\text{O}_{15}$ , and hex BSC, implying that hex BSCF exhibits higher OER catalytic activity.

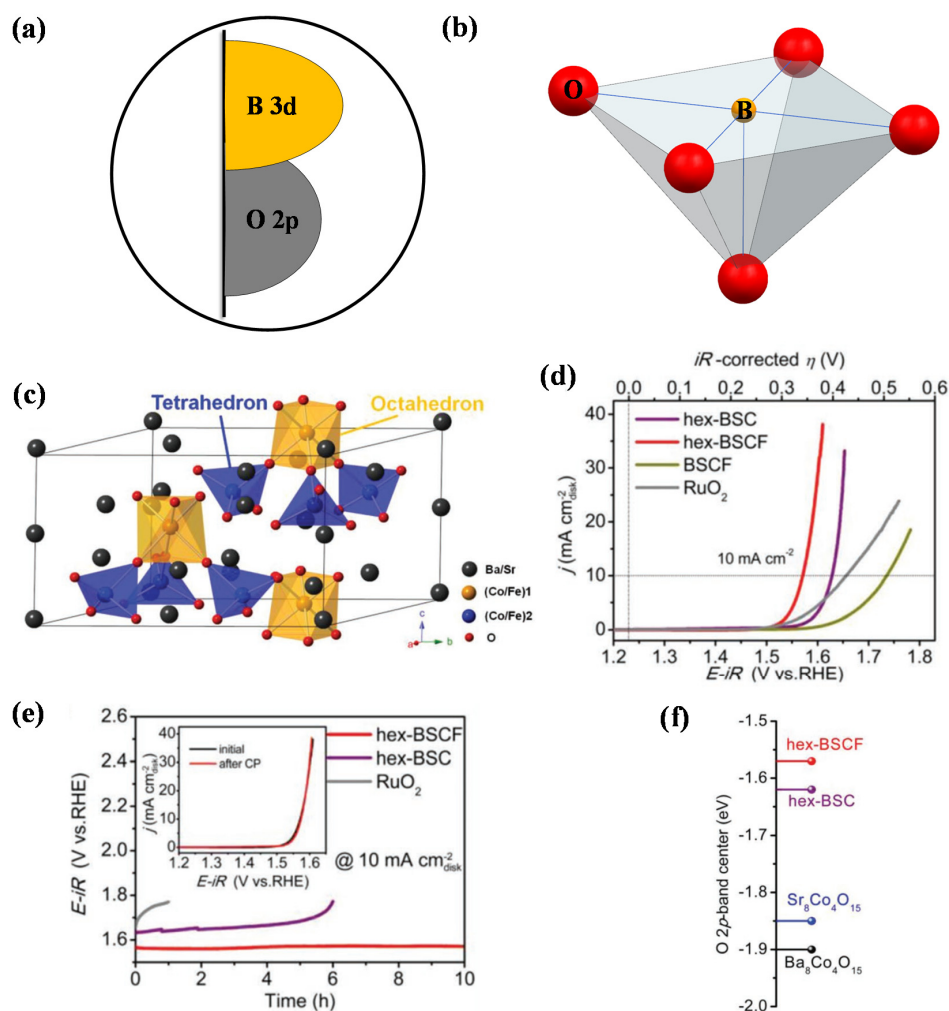


**Figure 8.** (a) Electronic structure of perovskites. (b)  $\text{BO}_5$  configuration. (c) Perspective view of the crystal structure of the hex-BSCF. (d) Capacitance- and ohmic resistance-corrected polarization curves of hex-BSC, hex-BSCF, BSCF, and  $\text{RuO}_2$  catalysts in an  $\text{O}_2$ -saturated 0.1 M KOH solution at a scan rate of  $10 \text{ mV s}^{-1}$ . (e) Chronopotentiometric (CP) curves of the hex-BSCF, hex-BSC, and  $\text{RuO}_2$  catalysts at  $10 \text{ mA cm}^{-2}_{\text{disk}}$ . The inset in (e) is the polarization curves of the hex-BSCF before and after the CP test. (f) Calculated O  $2p$ -band center relative to the Fermi level. Reproduced with permission from ref. [97], Copyright 2019, Wiley.

Recently, a number of *3d* transition metals (e.g., Mn, Fe, Co, Ni, and Cu), *4d* transition metals (e.g., Mo, Nb, and Pd), and *5d* transition metals (e.g., Hf, Ta, and W) have been doped into perovskite oxides, which are active toward OER/HER for water splitting [98]. For instance, the  $\text{SrNb}_{0.1}\text{Co}_{0.7}\text{Fe}_{0.2}\text{O}_{3-\delta}$  (SNCF) perovskite exhibits excellent OER intrinsic activity which is higher than that of the  $\text{IrO}_2$  catalyst and the well-known BSCF perovskite in an alkaline solution [99]. From a practical point of view, Fe-based materials are appealing in the family of perovskites considering that Fe metal is earth-abundant, inexpensive, and less toxic than Co and Ni metals, but Fe-based perovskite oxides traditionally have poor activity and unfavorable durability for OER/HER [32,100]. However, recent research showed that the OER/HER activity of Fe-based perovskites could be improved by proper B-site ion doping, such as Zr, Cu, Co, Ni, Mo, and Sn [98,101–103]. For instance, by a small amount of cobalt doping, both the catalytic activity and stability of  $\text{LaFeO}_3$  are further improved, with activity comparing favorably to or even outperforming Co-/Ni-rich perovskite catalysts [101]. Mo doping in perovskites was also beneficial for the OER/HER catalytic activity [104], such as for  $\text{SrCo}_{0.7}\text{Fe}_{0.25}\text{Mo}_{0.05}\text{O}_{3-\delta}$  [105],  $\text{Sr}_2\text{Fe}_{1.5-x-y}\text{Co}_x\text{Ni}_y\text{Mo}_{0.5}\text{O}_{6-\delta}$  [98], and  $\text{Sr}_2\text{Fe}_{1.5}\text{Mo}_{0.5}\text{O}_{6-\delta}$  [106].

The doping of non-metallic elements such as phosphorus (P), sulfur (S), boron (B), and silicon (Si) signifies a departure from the conventional doping route which can be used to stabilize the structure of perovskite oxides and significantly enhance the oxygen ionic conductivity [107–109]. For instance, metalloid Si, the second most abundant element in the earth's crust, is doped into a Fe-based perovskite oxide ( $\text{SrFeO}_{3-\delta}$ ) to obtain  $\text{SrFe}_{0.9}\text{Si}_{0.1}\text{O}_{3-\delta}$  as a highly efficient OER catalyst.  $\text{SrFe}_{0.9}\text{Si}_{0.1}\text{O}_{3-\delta}$  exhibits an approximately threefold growth in OER activity relative to  $\text{SrFeO}_{3-\delta}$  [109]. This enhancement can be ascribed to a structural transition from tetragonal to cubic symmetry upon Si-doping, which brings about an optimized Fe oxidation state, rich oxygen vacancies, and a fast charge transfer, which are beneficial to the OER catalysis. Analogously, Slater's group also performed a series of studies to demonstrate the successful incorporation of non-metal elements into the B-site cations of the perovskite oxides [107,110,111]. For example, the silicon doping into  $\text{Ba}_2\text{In}_2\text{O}_5$  leads to a significant enhancement in the oxide ion conductivity, which indicates that silicon is incorporated into the structure, leading to the conversion from an ordered brownmillerite-type structure to a disordered perovskite-type structure, with the disordering oxygen vacancy benefiting the conductivity enhancement [107].

Despite considerable efforts, the OER/HER electrocatalytic performances of most perovskite oxides are still inferior to those of commercial  $\text{IrO}_2/\text{RuO}_2$  or Pt/C catalysts. Recent studies have shown that doping a small number of precious metals (i.e., Pt, Ru, and Ir) in perovskites can significantly improve their activity and stability [61,112–115]. For instance, Wang et al. prepared a series of  $\text{LaCo}_{1-x}\text{Pt}_x\text{O}_{3-\delta}$  ( $x = 0, 0.02, 0.04, 0.06,$  and  $0.08$ ) perovskite oxides. Among them, the  $\text{LaCo}_{0.94}\text{Pt}_{0.06}\text{O}_{3-\delta}$  (LCP6) catalyst exhibits good stability and presents more activity at a lower overpotential of 454 mV (at  $10 \text{ mA cm}^{-2}$ ), a lower Tafel slope value of  $86 \text{ mV dec}^{-1}$ , and a higher mass activity of  $44.4 \text{ A g}^{-1}$  for OER; it also displays a lower overpotential of 294 mV (at  $-10 \text{ mA cm}^{-2}$ ), a lower Tafel slope value of  $148 \text{ mV dec}^{-1}$ , and a higher mass activity of  $-34.5 \text{ A g}^{-1}$  for HER in alkaline media. [112]. The  $e_g$  orbital filling of LCP6 is calculated to be 1.29, which is the closest to 1.2. Similarly, Yan et al. synthesized perovskite  $(\text{La}_{0.8}\text{Sr}_{0.2})_{0.95}\text{Mn}_{0.95}\text{Ir}_{0.05}\text{O}_3$  (LSMI) nanoparticles, which exhibit a significant enhancement in the OER electrocatalytic activity and durability compared to  $\text{La}_{0.8}\text{Sr}_{0.2}\text{MnO}_3$  (LSM) [113]. The LSMI with the B-site Ir-doping has a larger lattice, a lower valence state of the transition metal, and weaker metal–OH bonding compared with LSM; therefore, it increases the concentration of oxygen vacancy and enhances OER activity.

Recently, in addition to the A- and/or B-site doping/substituting, the partial possession of O-site anions by another element, such as  $\text{H}^-$  [116],  $\text{S}^{2-}$  [117],  $\text{N}^{3-}$  [118],  $\text{Cl}^-$  [119], or  $\text{F}^-$  [120], has been reported to exhibit many interesting properties. For instance, Yamamoto et al. prepared the oxyhydride perovskite  $\text{EuTiO}_{3-x}\text{H}_x$  ( $x \leq 0.3$ ) by a low temperature  $\text{CaH}_2$  reduction of the pyrochlore  $\text{Eu}_2\text{Ti}_2\text{O}_7$  and the perovskite  $\text{EuTiO}_3$  (Figure 9a) [116]. There may be certain

conduction mechanisms manifested best by hydrogen, such as quantum tunneling at low temperatures or coordinated proton/electron movement at high temperatures. Many new electronic/magnetic properties may also be conceived given the strong superexchange interaction found in  $\text{LaSrCoO}_3\text{H}_{0.7}$  [121]. Wang et al. prepared a stable cubic perovskite  $\text{SrCoO}_{2.85-\delta}\text{F}_{0.15}$  with excellent OER electrochemical performance, with a 380 mV overpotential at  $10 \text{ mA cm}^{-2}$  and six-times-higher mass activity at 420 mV through a simple F-doping (Figure 9b) [120]. The conspicuous enhancement of the OER performance for the  $\text{SrCoO}_{2.85-\delta}\text{F}_{0.15}$  catalyst may be attributed to the improvement of the electronic conductivity on account of the structure change from a 2H- to a 3C-perovskite after F-doping. Another factor may be the increased number of reactive oxygen species ( $\text{O}_2^{2-}/\text{O}^-$  species), which contributes to its enhanced OER activity. So far, studies on the anion doping of perovskite oxides for electrocatalysis are relatively scarce, so this is a topic of research value.

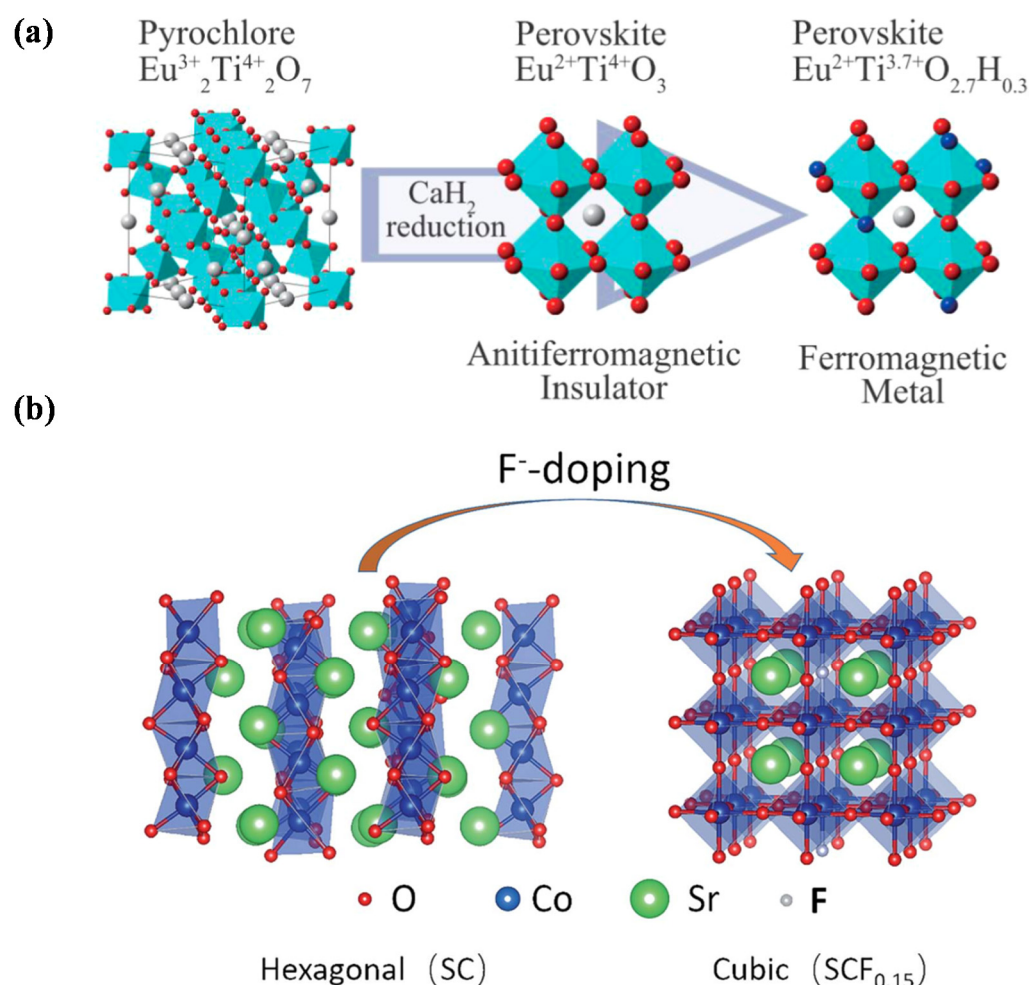


**Figure 9.** (a) The oxyhydroxide perovskite  $\text{EuTiO}_{3-x}\text{H}_x$  ( $x \leq 0.3$ ) prepared by a low temperature  $\text{CaH}_2$  reduction of pyrochlore  $\text{Eu}_2\text{Ti}_2\text{O}_7$  and perovskite  $\text{EuTiO}_3$ . Reproduced with permission from ref. [116], Copyright 2015, American Chemical Society. (b) Schematic presentation of the structural transition from the hexagonal structure to the cubic structure. Reproduced with permission from ref. [120], Copyright 2019, Royal Society of Chemistry.

#### 4.1.2. Defect Engineering

Great research efforts have been devoted to optimizing the performance of perovskite oxides, among which the defect engineering approach has proven its effectiveness in improving the intrinsic activity by regulating the electronic structure and inducing vacancy formation [16,122]. For  $\text{ABO}_3$  perovskite oxides, the A/B cation ratio deviates from 1 within a certain range (0.9~1.1), and the structure can remain stable due to the high structural

tolerance of the perovskite lattice [123]. The surface defect engineering of perovskites can be realized by the selective dissolution of A-site cations. Exsolutions emerge preferentially on the surface when highly A-site-deficient perovskites ( $A/B < 1$ ) are employed. A-site deficiency could serve as a general driving force to trigger B-site exsolution; therefore, A-site deficiency is the natural choice for designing systems that exsolve the B-sites [124]. For example, Islam et al. prepared the  $\text{Sr}_{0.95}\text{Nb}_{0.1}\text{Co}_{0.9-x}\text{Ni}_x\text{O}_{3-\delta}$  perovskite oxide, which exhibits improved ORR, OER, and HER activity at lower overpotentials [125].

The oxygen vacancy defect is another crucial parameter in improving the electrocatalysis of oxygen on the metal oxide surfaces, whereby they may control the physical parameters of ionic diffusion rates and reflect the underlying electronic structure [126]. The degree of vacancy formation reflects the relative position of the transition metal 3d-band and the oxygen 2p-band in the lattice, the more covalent system generating the higher vacancy concentration. After careful adjustment of the oxygen defects, the performances of the perovskite catalysts have been improved—e.g., greater conductivity, better thermal expansion, and higher battery performance. Plenty of perovskite oxides containing oxygen vacancies are synthesized by different methods and used for electrocatalytic water splitting [58,64,90,106,112,125,127]. The content of oxygen vacancy is closely correlated with the catalytic activity. For example,  $\text{NdBaMn}_2\text{O}_{5.5}$  exhibits a better overall water splitting performance than  $\text{NdBaMn}_2\text{O}_{5.5-\delta}$  and  $\text{NdBaMn}_2\text{O}_{5.5+\delta}$  [127].

#### 4.2. Surface Modification

Regulating the nature and number of surface-active sites on perovskite oxides is a proven promising strategy to improve catalytic activity. Many surface modification methods have been developed to adjust the surface chemical properties of catalyst materials, such as mussel-inspired chemistry [128], acid/base treatment [129], and so on, which show promising potential for the manufacture of catalysts. For example, Yang et al. modified the surface of the  $\text{La}_{0.8}\text{Sr}_{0.2}\text{CoO}_3$  perovskite by diluted oxalic etching to generate more surface Lewis acid sites, and it features a low-valence state with reactive dangling bonds and simultaneously enables more active oxygen species and favorable reactant adsorption and dissociation, consequently improving propane oxidation activity [130].

Recently, surface hetero-phase modification has been introduced to improve the electrocatalysis performance of the matrix phase by effectively utilizing the activity of the additive phase and the modified electronic structure at the heterointerface of the hybrid catalysts [131]. Numerous studies have dramatically proven the beneficial effect of surface modification. For instance, recent work by Li verified the enhancement of the oxygen evolution activity of a perovskite ( $\text{La}_{0.8}\text{Sr}_{0.2}\text{Co}_{0.95}\text{MnO}_{3-\delta}$ ) electrode by Co phase surface modification [132]. The surface modification of  $(\text{La,Sr})\text{MnO}_3$  with  $\text{CoO}(\text{OH})$  or  $\text{Co}_3\text{O}_4$  by the hydrothermal method exhibits synergistically improved OER mass and specific activity over the individual phase. Perovskite  $\text{Sr}_{0.9}\text{Y}_{0.1}\text{CoO}_{3-\delta}$  nanorods modified with  $\text{CoO}$  nanoparticles provide an improved electrochemical performance toward OER/ORR for lithium–oxygen batteries [133]. Furthermore, a mixed Co/Fe oxyhydroxide onto the surface of BSCF was obtained by a chemical precipitation/coprecipitation method and also exhibits enhanced OER activity [134].

Additionally, surface reconstruction is an efficient and simple method to further improve the catalytic activity by building specific surfaces. For example, Zhao et al. reported that the surface reconstruction of LSCF-2 could be completed by immersing as-synthesized  $\text{La}_{0.8}\text{Sr}_{0.2}\text{Co}_{0.8}\text{Fe}_{0.2}\text{O}_{3-\delta}$  (LSCF-0) in an aqueous solution of reductive  $\text{NaBH}_4$  for 1.0 h (Figure 10a) [135]. During the surface reconstruction, the smooth crystalline surface of as-synthesized LSCF-0 (Figure 10b) is converted into a rough amorphous layer consisting of nanosized particles of 20 nm (Figure 10c), and  $\text{Co}^{3+}$  was reduced to  $\text{Co}^{2+}$ . Benefiting from this conversion, the surface-reconstructed LSCF-2 exhibits excellent OER catalytic activity, with an overpotential of 248 mV (10 mA  $\text{cm}^{-2}$ ) and a Tafel slope of 51 mV  $\text{dec}^{-1}$  in alkaline media. A recent study by Sun et al. proposed a refined A-site management strategy for perovskite oxides which facilitates the surface reconstruction of

the B-site element-based active phase to enhance OER performance (Figure 10d) [136]. The electrocatalyst  $\text{LaNiO}_3$  displays a dynamic reconstruction feature during OER, with the growth of a self-assembled  $\text{NiOOH}$  active layer. Such reconstructed surface region likely contains a high number of structural domains with corner-shared and under-coordinated  $\text{IrO}_x$  octahedrons, and it is responsible for the high activity. Moreover, Grimaud et al. observed drastic surface reconstruction and iridium migration from the bulk to the surface with the help of transmission electron microscopy [137].

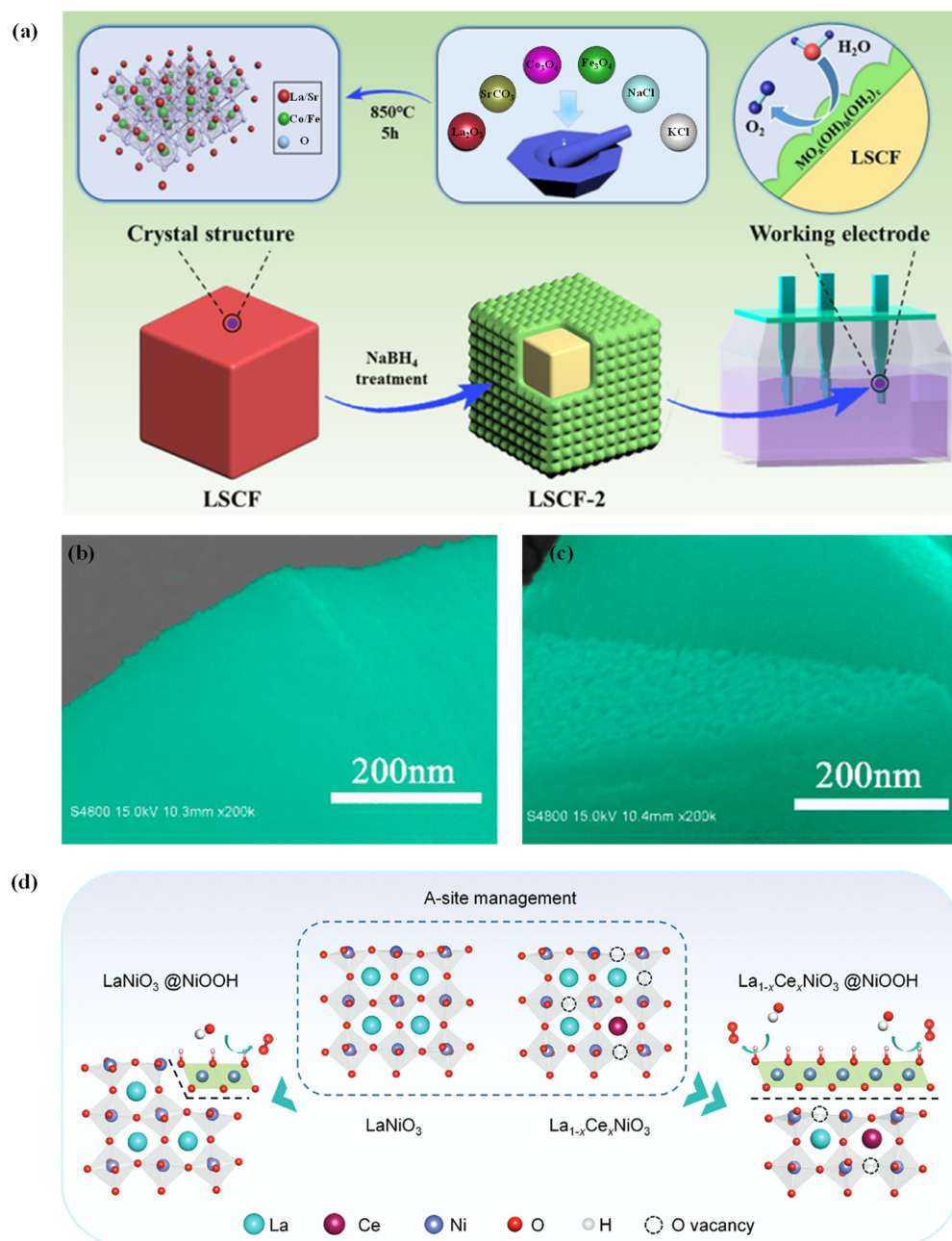


**Figure 10.** (a) A schematic that illustrates the surface reconstruction over the LSCF-0 surface. SEM images of (b) LSCF-0 and (c) LSCF-2. Reproduced with permission from ref. [135], Copyright 2019, American Chemical Society. (d) The surface reconstruction process of  $\text{La}_{1-x}\text{Ce}_x\text{NiO}_3$  to the active structure of  $\text{NiOOH}$  by the A-site management of the Ce substitution strategy. Reproduced with permission from ref. [136], Copyright 2021, Wiley.

Exsolution represents another strategy for the surface modification of perovskite nanoparticles. For instance, Lee et al. explored the Ni-exsolved  $\text{CaTiO}_3$  after the replacement of Ca by Ni, which showed large active site areas and a strong metal-support interaction (SMSI) leading to higher geometric activity and stability for OER [138]. Furthermore, a great deal of effort has been made to construct noble metal/perovskite oxide composites through the control of the exsolution to obtain excellent thermal stability and transport properties [139–141]. For example, the  $\text{RuO}_2/\text{La}_{0.9}\text{Fe}_{0.92}\text{Ru}_{0.08}\text{O}_3$  (LFRO) composites were prepared by the exsolution of a low Ru-substituted A-site-deficient perovskite [141]. In this process, pure Ru NPs are in situ exsolved from the LFRO via a relatively low heat treatment temperature in 5%  $\text{H}_2/\text{Ar}$ , and then the exsolved Ru NPs are oxidized to  $\text{RuO}_2$  for OER applications.

Additionally, other approaches such as solvent-induced surface hydroxylation are proposed to optimize the absorption energy of the intermediates on the active sites of perovskites. For example, the layered perovskite  $\text{Sr}_3\text{FeCoO}_{7-\delta}$  was presented through a facile approach of a solvent treatment to hydroxylate the surface, which exhibits significantly improved OER activity [21]. Furthermore, Yang et al. proposed a “dual strategy” in which tuning the electronic properties of the oxides, such as  $\text{La}_{1-x}\text{Sr}_x\text{CoO}_{3-\delta}$ , can be dissociated from the use of surface functionalization with the phosphate ion groups (Pi) that enhances the interfacial proton transfer [22]. This work also demonstrated that the Pi surface functionalization selectivity enhances the activity when the OER kinetics are limited by the proton transfer.

#### 4.3. Nanostructure and Morphology Control

Because of the high crystallization temperature, perovskite oxides typically present large particle sizes, resulting in a small surface-to-bulk ratio. Nanostructure engineering has been widely adapted to improve the catalytic activity of perovskite-type electrocatalysts. The high surface area (surface/volume ratio) and adequate active sites in nanosized perovskite materials are favorable to improving the catalytic activity by building nanosized surfaces, such as  $\text{SrNb}_{0.1}\text{Co}_{0.7}\text{Fe}_{0.2}\text{O}_{3-\delta}$  nanorods [8],  $\text{PrBa}_{0.5}\text{Sr}_{0.5}\text{Co}_{1.5}\text{Fe}_{0.5}\text{O}_{5+\delta}$  nanofiber [142], and nanoporous  $\text{LaMO}_3$  ( $M = \text{Co}, \text{Mn}, \text{Ni}, \text{or Cr}$ ) [91]. Apart from that, Lee et al. reported  $\text{La}_{1-x}\text{Sr}_x\text{Co}_{0.2}\text{Fe}_{0.8}\text{O}_{3-\delta}$  perovskite oxide catalysts with a unique three-dimensional (3D) fiber web structure that increases the high-contact area by trapping soot in the unique pore structure for effective catalytic activity [143]. However, these unique nanostructures may be coarsened and blocked during electrocatalytic reactions, especially under high-temperature conditions, causing catalyst degradation. Therefore, it is very important to find a suitable nanometric size that can balance the electrocatalytic activity and stability. The partial properties and electrocatalytic activities of different perovskite materials reported in the literature are summarized in Table 1.

**Table 1.** Summary of the properties and electrocatalytic activities of different perovskite materials reported in the literature.

Perovskite Materials	Morphology	Overpotential at 10 mA cm <sup>-2</sup> for OER (mV)	Tafel Slope for OER (mV dec <sup>-1</sup> )	Ref.
V-LCO/ $\text{Co}_3\text{O}_4$	nanosheets with holes	354	73	[19]
$\text{Sr}_2\text{Fe}_{0.8}\text{Co}_{0.2}\text{Mo}_{0.6}\text{Co}_{0.4}\text{O}_{6-\delta}$	particles	345	60	[47]
$\text{IrO}_x/\text{SrIrO}_3$	thin films	270	—	[61]
$(\text{PrBa}_{0.5}\text{Sr}_{0.5})_{0.95}\text{Co}_{1.5}\text{Fe}_{0.5}\text{O}_{5+\delta}/3\text{DNG}$	mesoporous	320	74	[68]
BSCF LSMO NSTO	thin films	330	50	[84]
Mg-doped $\text{LaNiO}_3$	nanofibers	450	95	[88]
hexagonal $\text{Ba}_4\text{Sr}_4(\text{Co}_{0.8}\text{Fe}_{0.2})_4\text{O}_{15}$	—	340	47	[97]
$\text{LaCo}_{0.94}\text{Pt}_{0.06}\text{O}_{3-\delta}$	particles	454	86	[112]
$\text{SrCoO}_{2.85-\delta}\text{F}_{0.15}$	—	380	60	[120]
LSCF-2	nanoparticles	248	51	[135]

## 5. Conclusions and Outlook

Recent years have witnessed a growing interest in the research of catalysts for electrochemical water splitting. The primary goal is to exploit the high-performance, cost-effective, and abundant electrocatalysts for water splitting. In this article, we have reviewed the general mechanisms of electrochemical water splitting, the superiority of perovskite oxides as electrocatalysts for water splitting, and the performance improvement strategies for perovskite oxides. Despite the obvious improvement, the development of perovskite catalysts for electrochemical water splitting is still at an early stage, and many challenges remain.

Given the compositional and structural flexibility of perovskite oxides, great opportunities lie ahead in the pursuit of improved electrocatalysts. Here, we list possible research directions to achieve this goal. Firstly, the relationship between the composition, crystal structure (especially the electronic structure of perovskite oxides), and catalytic performance needs to be researched deeply to obtain an adequate understanding. The A-, B-, and/or O-site doping/substituting and deficiency creation in  $ABO_3$  perovskite oxides have large characteristic effects on the electronic structure and coordination chemistry. Several related parameters are used to evaluate the properties of materials, including the  $e_g$  electron ( $\sigma^*$  orbital occupation), the B-O bond strength, the spin state, the  $d$ -band center of the transition metal, and the  $p$ -band center of the oxygen relative to the Fermi level. Based on this, a better understanding can be facilitated by combining experimental tools with theoretical methods (e.g., DFT calculations). Secondly, long-term stability cannot be ignored in terms of its application in practical production. Of special interest is the elements leaching from the surface layers in operation. This phenomenon may improve the electrocatalytic activity or deactivate the catalysts. In situ testing may be a viable option during the reaction processes. Thirdly, novel design strategies are very important for the morphology improvement and performance enhancement of perovskite oxide. As everyone knows, the high specific surface area is one of the key factors in obtaining excellent electrocatalytic performance, which is closely related to the synthesis method. Further, the large-scale synthesis of perovskites is also a great challenge for researchers, since most studies are still limited to the lab scale.

With the rapid development of perovskite oxides in the field of electrocatalytic water splitting, there is still a large number of perovskite oxides and derivatives that are theoretically predicted to exist but have not been explored experimentally. Therefore, perovskite oxides still have a very broad research space and even extend to a wider range of chemical reactions. This is extremely challenging.

**Author Contributions:** Conceptualization, C.S.; methodology, C.S.; validation, C.S. and W.Z.; formal analysis, Z.Y.; investigation, J.C.; resources, X.H.; writing—original draft preparation, C.S.; writing—review and editing, Q.L.; visualization, E.G.; supervision, J.L.; project administration, C.S.; funding acquisition, C.S., Q.L. and E.G. All authors have read and agreed to the published version of the manuscript.

**Funding:** This research was funded by the National Natural Science Foundation of China, grant number 51901108; the Natural Science Foundation of Shandong Province, China, grant number ZR201808190072; the Universities Twenty Foundational Items of Jinan City, grant number 2019GXRC036; and the Youth Innovation and Technology Support Plan of Shandong Province, grant number 2020KJA008.

**Institutional Review Board Statement:** Not applicable.

**Informed Consent Statement:** Not applicable.

**Data Availability Statement:** Not applicable.

**Conflicts of Interest:** The authors declare no conflict of interest.

## References

1. Noah, K.; Felix, L.; Daniel, M.K. Energy storage deployment and innovation for the clean energy transition. *Nat. Energy* **2017**, *2*, 17125.
2. Hosseini, S.E.; Wahid, M.A. Hydrogen production from renewable and sustainable energy resources: Promising green energy carrier for clean development. *Renew. Sustain. Energy Rev.* **2016**, *57*, 850–866. [[CrossRef](#)]
3. Iain, S.; Daniel, S.; Anthony, V.A.; Paul, B.; Paul, E.D.; Paul, E.; Nilay, S.; Kate, R.W. The role of hydrogen and fuel cells in the global energy system. *Energy Environ. Sci.* **2019**, *12*, 463–491.
4. Sebastian, T.W.; Jakob, S.E.; Søren, B.V.; Flemming, B.B.; Winnie, L.E.; Kim, A.-P.; Cathrine, F.; Ib, C.; Peter, M.M. Electrified methane reforming: A compact approach to greener industrial hydrogen production. *Science* **2019**, *364*, 756–759.
5. Liu, M.; Sun, W.; Li, X.; Feng, S.; Ding, D.; Chen, D.; Liu, M.; Park, H.C. High-performance Ni-BaZr<sub>0.1</sub>Ce<sub>0.7</sub>Y<sub>0.1</sub>Yb<sub>0.1</sub>O<sub>3-δ</sub> (BZCYb) membranes for hydrogen separation. *Int. J. Hydrog. Energy* **2013**, *38*, 14743–14749. [[CrossRef](#)]
6. Oka, K.; Tsujimura, O.; Suga, T.; Nishide, H.; Jensen, B.W. Light-assisted electrochemical water-splitting at very low bias voltage using metal-free polythiophene as photocathode at high pH in a full-cell setup. *Energy Environ. Sci.* **2018**, *11*, 1335–1342. [[CrossRef](#)]
7. Pearre, N.; Swan, L. Combining wind, solar, and in-stream tidal electricity generation with energy storage using a load-perturbation control strategy. *Energy* **2020**, *203*, 117898. [[CrossRef](#)]
8. Zhu, Y.; Zhou, W.; Zhong, Y.; Bu, Y.; Chen, X.; Zhong, Q.; Liu, M.; Shao, Z. A perovskite nanorod as bifunctional electrocatalyst for overall water splitting. *Adv. Energy Mater.* **2017**, *7*, 1602122. [[CrossRef](#)]
9. Long, X.; Lin, H.; Zhou, D.; An, Y.; Yang, S. Enhancing full water-splitting performance of transition metal bifunctional electrocatalysts in alkaline solutions by tailoring CeO<sub>2</sub>-transition metal oxides-Ni nanointerfaces. *ACS Energy Lett.* **2018**, *3*, 290–296. [[CrossRef](#)]
10. Yu, L.; Zhou, H.; Sun, J.; Qin, F.; Yu, F.; Bao, J.; Yu, Y.; Chen, S.; Ren, Z. Cu nanowires shelled with NiFe layered double hydroxide nanosheets as bifunctional electrocatalysts for overall water splitting. *Energy Environ. Sci.* **2017**, *10*, 1820–1827. [[CrossRef](#)]
11. Yu, F.; Zhou, H.; Huang, Y.; Sun, J.; Qin, F.; Bao, J.; Goddard, W.A., III; Chen, S.; Ren, Z. High-performance bifunctional porous non-noble metal phosphide catalyst for overall water splitting. *Nat. Commun.* **2018**, *9*, 2551. [[CrossRef](#)] [[PubMed](#)]
12. Hou, Y.; Lohe, M.R.; Zhang, J.; Liu, S.; Zhuang, X.; Feng, X. Vertically oriented cobalt selenide/NiFe layered-double-hydroxide nanosheets supported on exfoliated graphene foil: An efficient 3D electrode for overall water splitting. *Energy Environ. Sci.* **2016**, *9*, 478–483. [[CrossRef](#)]
13. Han, N.; Liu, P.; Jiang, J.; Ai, L.; Shao, Z.; Liu, S. Recent advances in nanostructured metal nitrides for water splitting. *J. Mater. Chem. A* **2018**, *6*, 19912–19933. [[CrossRef](#)]
14. Han, N.; Yang, K.R.; Lu, Z.; Li, Y.; Xu, W.; Gao, T.; Cai, Z.; Zhang, Y.; Batista, V.S.; Liu, W.; et al. Nitrogen-doped tungsten carbide nanoarray as an efficient bifunctional electrocatalyst for water splitting in acid. *Nat. Commun.* **2018**, *9*, 924. [[CrossRef](#)] [[PubMed](#)]
15. Hua, B.; Li, M.; Luo, J.L. A facile surface chemistry approach to bifunctional excellence for perovskite electrocatalysis. *Nano Energy* **2018**, *49*, 117–125. [[CrossRef](#)]
16. Zong, R.; Fang, Y.; Zhu, C.; Zhang, X.; Wu, L.; Hou, X.; Tao, Y.; Shao, J. Surface defect engineering on perovskite oxides as efficient bifunctional electrocatalysts for water splitting. *ACS Appl. Mater. Interfaces* **2021**, *13*, 42852–42860. [[CrossRef](#)]
17. Kim, J.H.; Yoo, S.; Murphy, R.; Chen, Y.; Ding, Y.; Pei, K.; Zhao, B.; Kim, G.; Choi, Y.; Liu, M.L. Promotion of oxygen reduction reaction on a double perovskite electrode by a water-induced surface modification. *Energy Environ. Sci.* **2021**, *14*, 1506–1516. [[CrossRef](#)]
18. Hua, B.; Li, M.; Sun, Y.F.; Zhang, Y.Q.; Yan, N.; Chen, J.; Thundat, T.; Li, J.; Luo, J.L. A coupling for success: Controlled growth of Co/CoOx nanoshoots on perovskite mesoporous nanofibres as high-performance trifunctional electrocatalysts in alkaline condition. *Nano Energy* **2017**, *32*, 247–254. [[CrossRef](#)]
19. Zhang, J.; Li, J.; Zhong, C.; Xi, P.; Chao, D.; Gao, D. Surface-electronic-structure reconstruction of perovskite via double-cation gradient etching for superior water oxidation. *Nano Lett.* **2021**, *21*, 8166–8174. [[CrossRef](#)]
20. Gui, L.Q.; Pan, G.H.; Ma, X.; You, M.S.; He, B.B.; Yang, Z.H.; Sun, J.; Zhou, W.; Xu, J.M.; Zhao, L. In-situ exsolution of CoNi alloy nanoparticles on LiFe<sub>0.8</sub>Co<sub>0.1</sub>Ni<sub>0.1</sub>O<sub>2</sub> parent: New opportunity for boosting oxygen evolution and reduction reaction. *Appl. Surf. Sci.* **2021**, *543*, 148817. [[CrossRef](#)]
21. Xu, K.L.; Song, F.; Gu, J.; Xu, X.; Liu, Z.N.; Hu, X.L. Solvent-induced surface hydroxylation of a layered perovskite Sr<sub>3</sub>FeCoO<sub>7-δ</sub> for enhanced oxygen evolution catalysis. *J. Mater. Chem. A* **2018**, *6*, 14240–14245. [[CrossRef](#)]
22. Yang, C.Z.; Laberty-Robert, C.; Batuk, D.; Cibin, G.; Chadwick, A.V.; Pimenta, V.; Yin, W.; Zhang, L.T.; Tarascon, J.-M.; Grimaud, A. Phosphate ion functionalization of perovskite surfaces for enhanced oxygen evolution reaction. *J. Phys. Chem. Lett.* **2017**, *8*, 3466–3472. [[CrossRef](#)] [[PubMed](#)]
23. Wang, X.; Dai, J.; Zhou, C.; Guan, D.; Wu, X.; Zhou, W.; Shao, Z. Engineering charge redistribution within perovskite oxides for synergistically enhanced overall water splitting. *ACS Mater. Lett.* **2021**, *3*, 1258–1265. [[CrossRef](#)]
24. Wang, W.; Xu, M.; Xu, X.; Zhou, W.; Shao, Z. Perovskite oxide based electrodes for high-performance photoelectrochemical water splitting. *Angew. Chem. Int. Ed. Engl.* **2020**, *59*, 136–152. [[CrossRef](#)]
25. Xu, X.; Zhong, Y.; Shao, Z. Double perovskites in catalysis, electrocatalysis, and photo(electro)catalysis. *Trends Chem.* **2019**, *1*, 410–424. [[CrossRef](#)]

26. Yin, W.-J.; Weng, B.; Ge, J.; Sun, Q.; Li, Z.; Yan, Y. Oxide perovskites, double perovskites and derivatives for electrocatalysis, photocatalysis, and photovoltaics. *Energy Environ. Sci.* **2019**, *12*, 442–462. [[CrossRef](#)]
27. Xu, X.; Wang, W.; Zhou, W.; Shao, Z. Recent advances in novel nanostructuring methods of perovskite electrocatalysts for energy-related applications. *Small Methods* **2018**, *2*, 1800071. [[CrossRef](#)]
28. Hwang, J.; Rao, R.R.; Giordano, L.; Katayama, Y.; Yu, Y.; Shao-Horn, Y. Perovskites in catalysis and electrocatalysis. *Science* **2017**, *358*, 751–756. [[CrossRef](#)]
29. Jiao, Y.; Zheng, Y.; Jaroniec, M.; Qiao, S.Z. Design of electrocatalysts for oxygen- and hydrogen-involving energy conversion reactions. *Chem. Soc. Rev.* **2015**, *44*, 2060–2086. [[CrossRef](#)]
30. Li, Y.-F.; Selloni, A. Mechanism and activity of water oxidation on selected surfaces of pure and Fe-doped NiOx. *ACS Catal.* **2014**, *4*, 1148–1153. [[CrossRef](#)]
31. Fang, Y.H.; Liu, Z.P. Mechanism and tafel lines of electro-oxidation of water to oxygen on RuO<sub>2</sub>(110). *J. Am. Chem. Soc.* **2010**, *132*, 18214–18222. [[CrossRef](#)] [[PubMed](#)]
32. Suen, N.-T.; Hung, S.-F.; Quan, Q.; Zhang, N.; Xu, Y.-J.; Chen, H.M. Electrocatalysis for the oxygen evolution reaction: Recent development and future perspectives. *Chem. Soc. Rev.* **2017**, *46*, 337–365. [[CrossRef](#)] [[PubMed](#)]
33. Rossmeis, J.; Qu, Z.-W.; Zhu, H.; Kroes, G.-J.; Nørskov, J.K. Electrolysis of water on oxide surfaces. *J. Electroanal. Chem.* **2007**, *607*, 83–89. [[CrossRef](#)]
34. Hu, C.; Zhang, L.; Gong, J. Recent progress made in the mechanism comprehension and design of electrocatalysts for alkaline water splitting. *Energy Environ. Sci.* **2019**, *12*, 2620–2645. [[CrossRef](#)]
35. Li, L.; Wang, P.; Shao, Q.; Huang, X. Metallic nanostructures with low dimensionality for electrochemical water splitting. *Chem. Soc. Rev.* **2020**, *49*, 3072–3106. [[CrossRef](#)] [[PubMed](#)]
36. Tilak, B.V.; Chen, C.-P. Generalized analytical expressions for Tafel slope, reaction order and a.c. impedance for the hydrogen evolution reaction (HER): Mechanism of HER on platinum in alkaline media. *J. Appl. Electrochem.* **1993**, *23*, 631–640. [[CrossRef](#)]
37. Goodenough, J.B.; Manoharan, R.; Paranthaman, M. Surface protonation and electrochemical activity of oxides in aqueous solution. *J. Am. Chem. Soc.* **1990**, *112*, 2076–2082. [[CrossRef](#)]
38. Mefford, J.T.; Rong, X.; Abakumov, A.M.; Hardin, W.G.; Dai, S.; Kolpak, A.M.; Johnston, K.P.; Stevenson, K.J. Water electrolysis on La<sub>1-x</sub>Sr<sub>x</sub>CoO<sub>3-δ</sub> perovskite electrocatalysts. *Nat. Commun.* **2016**, *7*, 11053. [[CrossRef](#)]
39. Peng, M.; Huang, J.; Zhu, Y.; Zhou, H.; Hu, Z.; Liao, Y.-K.; Lai, Y.-H.; Chen, C.-T.; Chu, Y.-H.; Zhang, K.H.L.; et al. Structural anisotropy determining the oxygen evolution mechanism of strongly correlated perovskite nickelate electrocatalyst. *ACS Sustain. Chem. Eng.* **2021**, *9*, 4262–4270.
40. Dai, J.; Zhu, Y.; Tahini, H.A.; Lin, Q.; Chen, Y.; Guan, D.; Zhou, C.; Hu, Z.; Lin, H.-J.; Chan, T.-S.; et al. Single-phase perovskite oxide with super-exchange induced atomic-scale synergistic active centers enables ultrafast hydrogen evolution. *Nat. Commun.* **2020**, *11*, 5657. [[CrossRef](#)]
41. Parsons, R. The rate of electrolytic hydrogen evolution and the heat of adsorption of hydrogen. *Trans Faraday Soc.* **1958**, *54*, 1053–1063. [[CrossRef](#)]
42. Peña, M.A.; Fierro, J.L.G. Chemical structures and performance of perovskite oxides. *Chem. Rev.* **2001**, *101*, 1981–2018. [[CrossRef](#)] [[PubMed](#)]
43. Kobayashi, K.-I.; Kimura, T.; Sawada, H.; Terakura, K.; Tokura, Y. Room-temperature magnetoresistance in an oxide material with an ordered double-perovskite structure. *Nature* **1998**, *395*, 677–680. [[CrossRef](#)]
44. Maeno, Y.; Hashimoto, H.; Yoshida, K.; Nishizaki, S.; Fujita, T.; Bednorz, J.G.; Lichtenberg, F. Superconductivity in a layered perovskite without copper. *Nature* **1994**, *372*, 532–534. [[CrossRef](#)]
45. Locherer, T.; Dinnebier, R.; Kremer, R.K.; Greenblatt, M.; Jansen, M. Synthesis and properties of a new quadruple perovskite: A-site ordered PbMn<sub>3</sub>Mn<sub>4</sub>O<sub>12</sub>. *J. Solid State Chem.* **2012**, *190*, 277–284. [[CrossRef](#)]
46. Vasala, S.; Karppinen, M. A2B'B''O<sub>6</sub> perovskites: A review. *Prog. Solid State Chem.* **2015**, *43*, 1–36. [[CrossRef](#)]
47. Sun, H.; Xu, X.; Chen, G.; Zhou, Y.; Lin, H.-J.; Chen, C.-T.; Ran, R.; Zhou, W.; Shao, Z. Smart control of composition for double perovskite electrocatalysts toward enhanced oxygen evolution reaction. *ChemSusChem* **2019**, *12*, 5111–5116. [[CrossRef](#)] [[PubMed](#)]
48. Pelosato, R.; Cordaro, G.; Stucchi, D.; Cristiani, C.; Dotelli, G. Cobalt based layered perovskites as cathode material for intermediate temperature solid oxide fuel cells: A brief review. *J. Power Sources* **2015**, *298*, 46–67. [[CrossRef](#)]
49. Wang, Y.; Yang, Z.; Lu, F.; Jin, C.; Wu, J.; Shen, M.; Yang, R.; Chen, F. Carbon-coating functionalized La<sub>0.6</sub>Sr<sub>1.4</sub>MnO<sub>4+δ</sub> layered perovskite oxide: Enhanced catalytic activity for the oxygen reduction reaction. *RSC Adv.* **2015**, *5*, 974–980. [[CrossRef](#)]
50. Jung, K.-N.; Jung, J.-H.; Im, W.B.; Yoon, S.; Shin, K.-H.; Lee, J.-W. Doped lanthanum nickelates with a layered perovskite structure as bifunctional cathode catalysts for rechargeable metal-air batteries. *ACS Appl. Mater. Interfaces* **2013**, *5*, 9902–9907. [[CrossRef](#)]
51. Chen, C.-F.; King, G.; Dickerson, R.M.; Papin, P.A.; Gupta, S.; Kellogg, W.R.; Wu, G. Oxygen-deficient BaTiO<sub>3-δ</sub> perovskite as an efficient bifunctional oxygen electrocatalyst. *Nano Energy* **2015**, *13*, 423–432. [[CrossRef](#)]
52. Lee, H.; Gwon, O.; Choi, K.; Zhang, L.; Zhou, J.; Park, J.; Yoo, J.-W.; Wang, J.-Q. Enhancing bifunctional electrocatalytic activities via metal *d*-band center lift induced by oxygen vacancy on the subsurface of perovskites. *ACS Catal.* **2020**, *10*, 4664–4670. [[CrossRef](#)]
53. Abreu-Sepulveda, M.A.; Dhital, C.; Huq, A.; Li, L.; Bridges, C.A.; Paranthaman, M.P.; Narayanan, S.R.; Quesnel, D.J.; Tryk, D.A.; Manivannan, A. The influence of Fe substitution in lanthanum calcium cobalt oxide on the oxygen evolution reaction in alkaline media. *J. Electrochem. Soc.* **2016**, *163*, F1124–F1132. [[CrossRef](#)]

54. Zhu, Y.; Zhou, W.; Chen, Y.; Yu, J.; Liu, M.; Shao, Z. A high-performance electrocatalyst for oxygen evolution reaction:  $\text{LiCo}_{0.8}\text{Fe}_{0.2}\text{O}_2$ . *Adv. Mater.* **2015**, *27*, 7150–7155. [[CrossRef](#)] [[PubMed](#)]
55. Wang, T.; Fan, J.; Do-Thanh, C.-L.; Suo, X.; Yang, Z.; Chen, H.; Yuan, Y.; Lyu, H.; Yang, S.; Dai, S. Perovskite oxide-halide solid solutions: A platform for electrocatalysts. *Angew. Chem. Int. Ed.* **2021**, *26*, 9953–9958. [[CrossRef](#)]
56. Wang, L.; Stoerzinger, K.A.; Chang, L.; Zhao, J.; Li, Y.; Tang, C.S.; Yin, X.; Bowden, M.E.; Yang, Z.; Guo, H.; et al. Tuning bifunctional oxygen electrocatalysts by changing the A-site rare-earth element in perovskite nickelates. *Adv. Funct. Mater.* **2018**, *28*, 1803712. [[CrossRef](#)]
57. Xu, X.; Chen, Y.; Zhou, W.; Zhu, Z.; Su, C.; Liu, M.; Shao, Z. A perovskite electrocatalyst for efficient hydrogen evolution reaction. *Adv. Mater.* **2016**, *28*, 6442–6448. [[CrossRef](#)]
58. Li, X.; Zhao, H.; Liang, J.; Luo, Y.; Chen, G.; Shi, X.; Lu, S.; Gao, S.; Hu, J.; Liu, Q.; et al. A-site perovskite oxides: An emerging functional material for electrocatalysis and photocatalysis. *J. Mater. Chem. A* **2021**, *9*, 6650–6670. [[CrossRef](#)]
59. Si, W.; Wang, Y.; Peng, Y.; Li, J. Selective dissolution of A-site cations in  $\text{ABO}_3$  perovskites: A new path to high-performance catalysts. *Angew. Chem. Int. Ed. Engl.* **2015**, *127*, 8065–8068. [[CrossRef](#)]
60. Dai, L.; Lu, X.B.; Chu, G.H.; He, C.H.; Zhan, W.C.; Zhou, G.J. Surface tuning of  $\text{LaCoO}_3$  perovskite by acid etching to enhance its catalytic performance. *Rare Met.* **2020**, *40*, 555–562. [[CrossRef](#)]
61. Seitz, L.C.; Dickens, C.F.; Nishio, K.; Hikita, Y.; Montoya, J.; Doyle, A.; Kirk, C.; Vojvodic, A.; Hwang, H.Y.; Nørskov, J.K.; et al. A highly active and stable  $\text{IrOx}/\text{SrIrO}_3$  catalyst for the oxygen evolution reaction. *Science* **2016**, *353*, 1011–1014. [[CrossRef](#)]
62. Yan, D.; Li, Y.; Huo, J.; Chen, R.; Dai, L.; Wang, S. Defect chemistry of nonprecious-metal electrocatalysts for oxygen reactions. *Adv. Mater.* **2017**, *29*, 1606459. [[CrossRef](#)] [[PubMed](#)]
63. Grimaud, A.; Diaz-Morales, O.; Han, B.; Hong, W.T.; Lee, Y.L.; Giordano, L.; Stoerzinger, K.A.; Koper, M.T.M.; Shao-Horn, Y. Activating lattice oxygen redox reactions in metal oxides to catalyse oxygen evolution. *Nat. Chem.* **2017**, *9*, 457–465. [[CrossRef](#)] [[PubMed](#)]
64. Wu, X.; Yu, J.; Yang, G.; Liu, H.; Zhou, W.; Shao, Z. Perovskite oxide/carbon nanotube hybrid bifunctional electrocatalysts for overall water splitting. *Electrochim. Acta* **2018**, *286*, 47–54. [[CrossRef](#)]
65. Du, J.; Zhang, T.; Cheng, F.; Chu, W.; Wu, Z.; Chen, J. Nonstoichiometric perovskite  $\text{CaMnO}_{3-\delta}$  for oxygen electrocatalysis with high activity. *Inorg. Chem.* **2014**, *53*, 9106–9114. [[CrossRef](#)] [[PubMed](#)]
66. Zhou, W.; Sunarso, J. Enhancing bi-functional electrocatalytic activity of perovskite by temperature shock: A case study of  $\text{LaNiO}_{3-\delta}$ . *J. Phys. Chem. Lett.* **2013**, *4*, 2982–2988. [[CrossRef](#)]
67. Yan, J.; Lin, S.; Qiu, X.; Chen, H.; Li, K.; Yuan, Y.; Long, M.; Yang, B.; Gao, Y.; Zhou, C. Accelerated hole-extraction in carbon-electrode based planar perovskite solar cells by moisture-assisted post-annealing. *Appl. Phys. Lett.* **2019**, *114*, 103503. [[CrossRef](#)]
68. Bu, Y.; Jang, H.; Gwon, O.; Kim, S.H.; Joo, S.H.; Nam, G.; Kim, S.; Qin, Y.; Zhong, Q.; Kwak, S.K.; et al. Synergistic interaction of perovskite oxides and N-doped graphene in versatile electrocatalyst. *J. Mater. Chem. A* **2019**, *7*, 2048–2054. [[CrossRef](#)]
69. Farhang, Y.; Taheri-Nassaj, E.; Rezaei, M. Pd doped  $\text{LaSrCuO}_4$  perovskite nano-catalysts synthesized by a novel solid state method for CO oxidation and methane combustion. *Ceram. Int.* **2018**, *44*, 21499–21506. [[CrossRef](#)]
70. Ashok, A.; Kumar, A.; Bhosale, R.R.; Almomani, F.; Malik, S.S.; Suslov, S.; Tarlochan, F. Combustion synthesis of bifunctional  $\text{LaMO}_3$  ( $M = \text{Cr, Mn, Fe, Co, Ni}$ ) perovskites for oxygen reduction and oxygen evolution reaction in alkaline media. *J. Electroanal. Chem.* **2018**, *809*, 22–30. [[CrossRef](#)]
71. Xia, W.; Wu, H.; Xue, P.; Zhu, X. Microstructural, magnetic, and optical properties of Pr-doped perovskite manganite  $\text{La}_{0.67}\text{Ca}_{0.33}\text{MnO}_3$  nanoparticles synthesized via sol-gel process. *Nanoscale Res. Lett.* **2018**, *13*, 135. [[CrossRef](#)]
72. Zhang, R.; Dubouis, N.; Ben Osman, M.; Yin, W.; Sougrati, M.T.; Corte, D.A.D.; Giaume, D.; Grimaud, A. A dissolution/precipitation equilibrium on the surface of iridium-based perovskites controls their activity as oxygen evolution reaction catalysts in acidic media. *Angew. Chem. Int. Ed. Engl.* **2019**, *58*, 4571–4575. [[CrossRef](#)] [[PubMed](#)]
73. Saiduzzaman, M.; Yoshida, H.; Takei, T.; Yanagida, S.; Kumada, N.; Nagao, M.; Yamane, H.; Azuma, M.; Rubel, M.H.K.; Moriyoshi, C.; et al. Hydrothermal synthesis and crystal structure of a  $(\text{Ba}_{0.54}\text{K}_{0.46})_4\text{Bi}_4\text{O}_{12}$  double-perovskite superconductor with onset of the transition  $T_c \sim 30$  K. *Inorg. Chem.* **2019**, *58*, 11997–12001. [[CrossRef](#)] [[PubMed](#)]
74. Beckel, D.; Bieberle-Hütter, A.; Harvey, A.; Infortuna, A.; Muecke, U.P.; Prestat, M.; Rupp, J.L.M.; Gauckler, L.J. Thin films for micro solid oxide fuel cells. *J. Power Sources* **2007**, *173*, 325–345. [[CrossRef](#)]
75. Murauskas, T.; Kubilius, V.; Saltyte, Z.; Plausinaitiene, V. Metalorganic chemical vapor deposition and investigation of nonstoichiometry of undoped  $\text{BaSnO}_3$  and La-doped  $\text{BaSnO}_3$  thin films. *Thin Solid Film.* **2019**, *692*, 137575. [[CrossRef](#)]
76. Rehman, S.U.; Song, R.H.; Lim, T.H.; Park, S.J.; Hong, J.E.; Lee, J.W.; Lee, S.B. High-performance nanofibrous  $\text{LaCoO}_3$  perovskite cathode for solid oxide fuel cells fabricated via chemically assisted electrodeposition. *J. Mater. Chem. A* **2018**, *6*, 6987–6996. [[CrossRef](#)]
77. Zheng, Y.; Feng, X.; Lin, D.; Wu, E.; Luo, Y.; You, Y.; Huang, B.; Qian, Q.; Chen, Q. Insights into the low-temperature synthesis of  $\text{LaCoO}_3$  derived from  $\text{Co}(\text{CH}_3\text{COO})_2$  via electrospinning for catalytic propane oxidation. *Chin. J. Chem.* **2019**, *38*, 144–150. [[CrossRef](#)]
78. Vila-Fungueirino, J.M.; Gomez, A.; Antoja-Lleonart, J.; Gazquez, J.; Magen, C.; Noheda, B.; Carretero-Genevri, A. Direct and converse piezoelectric responses at the nanoscale from epitaxial  $\text{BiFeO}_3$  thin films grown by polymer assisted deposition. *Nanoscale* **2018**, *10*, 20155–20161. [[CrossRef](#)] [[PubMed](#)]

79. Ban, T.; Kaiden, T.; Ohya, Y. Hydrothermal synthesis of layered perovskite-structured metal oxides and cesium tungstate nanosheets. *Cryst. Growth Des.* **2019**, *19*, 6903–6910. [[CrossRef](#)]
80. Wang, S.; Liu, Q.; Zhao, Z.; Fan, C.; Chen, X.; Xu, G.; Wu, M.; Chen, J.; Li, J. Enhanced low-temperature activity of toluene oxidation over the rod-like  $\text{MnO}_2/\text{LaMnO}_3$  perovskites with alkaline hydrothermal and acid-etching treatment. *Ind. Eng. Chem. Res.* **2020**, *59*, 6556–6564. [[CrossRef](#)]
81. Singh, J.; Kumar, A.; Goutam, U.K.; Kumar, A. Microstructure and electrochemical performance of  $\text{La}_2\text{ZnMnO}_6$  nanoflakes synthesized by facile hydrothermal route. *Appl. Phys. A Mater.* **2019**, *126*, 11. [[CrossRef](#)]
82. Wang, S.; Wu, X.; Yuan, L.; Zhang, C.; Cui, X.; Lu, D. Hydrothermal synthesis, morphology, structure, and magnetic properties of perovskite structure  $\text{LaCr}_{1-x}\text{Mn}_x\text{O}_3$  ( $x = 0.1, 0.2, \text{ and } 0.3$ ). *CrystEngComm* **2018**, *20*, 3034–3042. [[CrossRef](#)]
83. Ogunniran, K.O.; Murugadoss, G.; Thangamuthu, R.; Periasamy, P. Evaluation of nanostructured  $\text{Nd}_{0.7}\text{Co}_{0.3}\text{FeO}_3$  perovskite obtained via hydrothermal method as anode material for Li-ion battery. *Mater. Chem. Phys.* **2020**, *248*, 122944. [[CrossRef](#)]
84. Risch, M.; Stoerzinger, K.A.; Maruyama, S.; Hong, W.T.; Takeuchi, I.; Shao-Horn, Y.  $\text{La}_{0.8}\text{Sr}_{0.2}\text{MnO}_{3-\delta}$  Decorated with  $\text{Ba}_{0.5}\text{Sr}_{0.5}\text{Co}_{0.8}\text{Fe}_{0.2}\text{O}_{3-\delta}$ : A bifunctional surface for oxygen electrocatalysis with enhanced stability and activity. *J. Am. Chem. Soc.* **2014**, *136*, 5229–5232. [[CrossRef](#)] [[PubMed](#)]
85. Ma, P.P.; Lei, N.; Yu, B.; Liu, Y.K.; Jiang, G.H.; Dai, J.M.; Li, S.H.; Lu, Q.L. Flexible supercapacitor electrodes based on carbon cloth-supported  $\text{LaMnO}_3/\text{MnO}$  nano-arrays by one-step electrodeposition. *Nanomaterials* **2019**, *9*, 1676. [[CrossRef](#)] [[PubMed](#)]
86. Wheeler, G.P.; Choi, K.S. Photoelectrochemical properties and stability of nanoporous p-type  $\text{LaFeO}_3$  photoelectrodes prepared by electrodeposition. *ACS Energy Lett.* **2017**, *2*, 2378–2382. [[CrossRef](#)]
87. Li, B.Q.; Tang, C.; Wang, H.F.; Zhu, X.L.; Zhang, Q. An aqueous preoxidation method for monolithic perovskite electrocatalysts with enhanced water oxidation performance. *Sci. Adv.* **2016**, *2*, e1600495. [[CrossRef](#)]
88. Bian, J.; Su, R.; Yao, Y.; Wang, J.; Zhou, J.; Li, F.; Wang, Z.L.; Sun, C. Mg doped perovskite  $\text{LaNiO}_3$  nanofibers as an efficient bifunctional catalyst for rechargeable zinc-air batteries. *ACS Appl. Energy Mater.* **2019**, *2*, 923–931. [[CrossRef](#)]
89. Vignesh, A.; Prabu, M.; Shanmugam, S. Porous  $\text{LaCo}_{1-x}\text{Ni}_x\text{O}_{3-\delta}$  nanostructures as an efficient electrocatalyst for water oxidation and for a zinc-air battery. *ACS Appl. Mater. Interfaces* **2016**, *8*, 6019–6031. [[CrossRef](#)]
90. Hua, B.; Li, M.; Zhang, Y.Q.; Sun, Y.F.; Luo, J.L. All-in-one perovskite catalyst: Smart controls of architecture and composition toward enhanced oxygen/hydrogen evolution reactions. *Adv. Energy Mater.* **2017**, *7*, 1700666. [[CrossRef](#)]
91. Si, C.; Zhang, C.; Sunarso, J.; Zhang, Z. Transforming bulk alloys into nanoporous lanthanum-based perovskite oxides with high specific surface areas and enhanced electrocatalytic activities. *J. Mater. Chem. A* **2018**, *6*, 19979–19988. [[CrossRef](#)]
92. Dai, X.P.; Li, R.J.; Yu, C.C.; Hao, Z.P. Unsteady-state direct partial oxidation of methane to synthesis gas in a fixed-bed reactor using  $\text{AFeO}_3$  ( $\text{A} = \text{La, Nd, Eu}$ ) perovskite-type oxides as oxygen storage. *J. Phys. Chem. B* **2006**, *110*, 22525–22531. [[CrossRef](#)] [[PubMed](#)]
93. Suntivich, J.; May, K.J.; Gasteiger, H.A.; Goodenough, J.B.; Shao-Horn, Y. A perovskite oxide optimized for oxygen evolution catalysis from molecular orbital principles. *Science* **2011**, *334*, 1383–1385. [[CrossRef](#)] [[PubMed](#)]
94. Azad, U.P.; Singh, M.; Ghosh, S.; Singh, A.K.; Ganesan, V.; Singh, A.K.; Prakash, R. Facile synthesis of BSCF perovskite oxide as an efficient bifunctional oxygen electrocatalyst. *Int. J. Hydrog. Energy* **2018**, *43*, 20671–20679. [[CrossRef](#)]
95. Cheng, X.; Fabbri, E.; Kim, B.; Nachttegaal, M.; Schmidt, T.J. Effect of ball milling on the electrocatalytic activity of  $\text{Ba}_{0.5}\text{Sr}_{0.5}\text{Co}_{0.8}\text{Fe}_{0.2}\text{O}_3$  towards the oxygen evolution reaction. *J. Mater. Chem. A* **2017**, *5*, 13130–13137. [[CrossRef](#)]
96. May, K.J.; Carlton, C.E.; Stoerzinger, K.A.; Risch, M.; Suntivich, J.; Lee, Y.-L.; Grimaud, A.; Shao-Horn, Y. Influence of oxygen evolution during water oxidation on the surface of perovskite oxide catalysts. *J. Phys. Chem. Lett.* **2012**, *3*, 3264–3270. [[CrossRef](#)]
97. Zhu, Y.; Tahini, H.A.; Hu, Z.; Chen, Z.-G.; Zhou, W.; Komarek, A.C.; Lin, Q.; Lin, H.-J.; Chen, C.-T.; Zhong, Y.; et al. Boosting oxygen evolution reaction by creating both metal ion and lattice-oxygen active sites in a complex oxide. *Adv. Mater.* **2020**, *32*, e1905025. [[CrossRef](#)]
98. Sun, H.; Hu, Z.; Xu, X.; He, J.; Dai, J.; Lin, H.-J.; Chan, T.-S.; Chen, C.-T.; Tjeng, L.H.; Zhou, W.; et al. Ternary phase diagram-facilitated rapid screening of double perovskites as electrocatalysts for the oxygen evolution reaction. *Chem. Mater.* **2019**, *31*, 5919–5926. [[CrossRef](#)]
99. Zhu, Y.; Zhou, W.; Chen, Z.-G.; Chen, Y.; Su, C.; Tade, M.O.; Shao, Z.  $\text{SrNb}_{0.1}\text{Co}_{0.7}\text{Fe}_{0.2}\text{O}_{3-\delta}$  perovskite as a next-generation electrocatalyst for oxygen evolution in alkaline solution. *Angew. Chem. Int. Ed. Engl.* **2015**, *127*, 3969–3973. [[CrossRef](#)]
100. Wu, Y.; Chen, M.; Han, Y.; Luo, H.; Su, X.; Zhang, M.-T.; Lin, X.; Sun, J.; Wang, L.; Deng, L.; et al. Fast and simple preparation of iron-based thin films as highly efficient water-oxidation catalysts in neutral aqueous solution. *Angew. Chem. Int. Ed. Engl.* **2015**, *127*, 4952–4957. [[CrossRef](#)]
101. Dai, J.; Zhu, Y.; Zhong, Y.; Miao, J.; Lin, B.; Zhou, W.; Shao, Z. Enabling high and stable electrocatalytic activity of iron-based perovskite oxides for water splitting by combined bulk doping and morphology designing. *Adv. Mater. Interfaces* **2019**, *6*, 1801317. [[CrossRef](#)]
102. Xu, X.; Su, C.; Zhou, W.; Zhu, Y.; Chen, Y.; Shao, Z. Co-doping strategy for developing perovskite oxides as highly efficient electrocatalysts for oxygen evolution reaction. *Adv. Sci.* **2016**, *3*, 1500187. [[CrossRef](#)] [[PubMed](#)]
103. Omari, E.; Omari, M. Cu-doped  $\text{GdFeO}_3$  perovskites as electrocatalysts for the oxygen evolution reaction in alkaline media. *Int. J. Hydrog. Energy* **2019**, *44*, 28769–28779. [[CrossRef](#)]
104. Zhang, X.; Yu, X.; Zhang, L.; Zhou, F.; Liang, Y.; Wang, R. Molybdenum phosphide/carbon nanotube hybrids as pH-universal electrocatalysts for hydrogen evolution reaction. *Adv. Funct. Mater.* **2018**, *28*, 1706523. [[CrossRef](#)]

105. Zhang, Z.; Chen, Y.; Dai, Z.; Tan, S.; Chen, D. Promoting hydrogen-evolution activity and stability of perovskite oxides via effectively lattice doping of molybdenum. *Electrochim. Acta* **2019**, *312*, 128–136. [[CrossRef](#)]
106. He, B.; Tan, K.; Gong, Y.; Wang, R.; Wang, H.; Zhao, L. Coupling amorphous cobalt hydroxide nanoflakes on  $\text{Sr}_2\text{Fe}_{1.5}\text{Mo}_{0.5}\text{O}_{5+\delta}$  perovskite nanofibers to induce bifunctionality for water splitting. *Nanoscale* **2020**, *12*, 9048–9057. [[CrossRef](#)] [[PubMed](#)]
107. Shin, J.F.; Apperley, D.C.; Slater, P.R. Silicon doping in  $\text{Ba}_2\text{In}_2\text{O}_5$ : Example of a beneficial effect of silicon incorporation on oxide ion/proton conductivity. *Chem. Mater.* **2010**, *22*, 5945–5948. [[CrossRef](#)]
108. Li, M.; Zhou, W.; Xu, X.; Zhu, Z.  $\text{SrCo}_{0.85}\text{Fe}_{0.1}\text{P}_{0.05}\text{O}_{3-\delta}$  perovskite as a cathode for intermediate-temperature solid oxide fuel cells. *J. Mater. Chem. A* **2013**, *1*, 13632–13639. [[CrossRef](#)]
109. Xu, X.; Chen, Y.; Zhou, W.; Zhong, Y.; Guan, D.; Shao, Z. Earth-abundant silicon for facilitating water oxidation over iron-based perovskite electrocatalyst. *Adv. Mater. Interfaces* **2018**, *5*, 1701693. [[CrossRef](#)]
110. Shin, J.F.; Orera, A.; Apperley, D.C.; Slater, P.R. Oxyanion doping strategies to enhance the ionic conductivity in  $\text{Ba}_2\text{In}_2\text{O}_5$ . *J. Mater. Chem.* **2011**, *21*, 874–879. [[CrossRef](#)]
111. Porras-Vazquez, J.M.; Kemp, T.F.; Hanna, J.V.; Slater, P.R. Synthesis and characterisation of oxyanion-doped manganites for potential application as SOFC cathodes. *J. Mater. Chem.* **2012**, *22*, 8287–8293. [[CrossRef](#)]
112. Wang, C.; Zeng, L.; Guo, W.; Gong, C.; Yang, J. Enhancing oxygen and hydrogen evolution activities of perovskite oxide  $\text{LaCoO}_3$  via effective doping of platinum. *RSC Adv.* **2019**, *9*, 35646–35654. [[CrossRef](#)] [[PubMed](#)]
113. Yan, L.; Lin, Y.; Yu, X.; Xu, W.; Salas, T.; Smallidge, H.; Zhou, M.; Luo, H.  $\text{La}_{0.8}\text{Sr}_{0.2}\text{MnO}_3$ -based perovskite nanoparticles with the A-site deficiency as high performance bifunctional oxygen catalyst in alkaline solution. *ACS Appl. Mater. Interfaces* **2017**, *9*, 23820–23827. [[CrossRef](#)] [[PubMed](#)]
114. Li, Q.; Wang, D.; Lu, Q.; Meng, T.; Yan, M.; Fan, L.; Xing, Z.; Yang, X. Identifying the activation mechanism and boosting electrocatalytic activity of layered perovskite ruthenate. *Small* **2020**, *16*, e1906380. [[CrossRef](#)] [[PubMed](#)]
115. Yu, J.; Wu, X.; Guan, D.; Hu, Z.; Weng, S.C.; Sun, H.; Song, Y.; Ran, R.; Zhou, W.; Ni, M.; et al. Monoclinic  $\text{SrIrO}_3$ : An easily synthesized conductive perovskite oxide with outstanding performance for overall water splitting in alkaline solution. *Chem. Mater.* **2020**, *32*, 4509–4517. [[CrossRef](#)]
116. Yamamoto, T.; Yoshii, R.; Bouilly, G.; Kobayashi, Y.; Fujita, K.; Kususe, Y.; Matsushita, Y.; Tanaka, K.; Kageyama, H. An antiferro-to-ferromagnetic transition in  $\text{EuTiO}_{3-x}\text{H}_x$  induced by hydride substitution. *Inorg. Chem.* **2015**, *54*, 1501–1507. [[CrossRef](#)]
117. Li, F.F.; Liu, D.R.; Gao, G.M.; Xue, B.; Jiang, Y.S. Improved visible-light photocatalytic activity of  $\text{NaTaO}_3$  with perovskite-like structure via sulfur anion doping. *Appl. Catal. B Environ.* **2015**, *166*, 104–111. [[CrossRef](#)]
118. Yajima, T.; Takeiri, F.; Aidzu, K.; Akamatsu, H.; Fujita, K.; Yoshimune, W.; Ohkura, M.; Lei, S.; Gopalan, V.; Tanaka, K.; et al. A labile hydride strategy for the synthesis of heavily nitrized  $\text{BaTiO}_3$ . *Nat. Chem.* **2015**, *7*, 1017–1023. [[CrossRef](#)]
119. Dai, H.X.; Ng, C.F.; Au, C. Perovskite-type halo-oxide  $\text{La}_{1-x}\text{Sr}_x\text{FeO}_{3-\delta}\text{X}_\sigma$  ( $\text{X}=\text{F}, \text{Cl}$ ) catalysts selective for the oxidation of ethane to ethene. *J. Catal.* **2000**, *189*, 52–62. [[CrossRef](#)]
120. Wang, W.; Yang, Y.; Huan, D.; Wang, L.; Shi, N.; Xie, Y.; Xia, C.; Peng, R.; Lu, Y. An excellent OER electrocatalyst of cubic  $\text{SrCoO}_{3-\delta}$  prepared by a simple F-doping strategy. *J. Mater. Chem. A* **2019**, *7*, 12538–12546. [[CrossRef](#)]
121. Hayward, M.A.; Cussen, E.J.; Claridge, J.B.; Bieringer, M.; Rosseinsky, M.J.; Kiely, C.J.; Blundell, S.J.; Marshall, I.M.; Pratt, F.L. The hydride anion in an extended transition metal oxide array:  $\text{LaSrCoO}_3\text{H}_{0.7}$ . *Science* **2002**, *295*, 1882–1884. [[CrossRef](#)]
122. Liu, H.; Ding, X.; Wang, L.; Ding, D.; Zhang, S.; Yuan, G. Cation deficiency design: A simple and efficient strategy for promoting oxygen evolution reaction activity of perovskite electrocatalyst. *Electrochim. Acta* **2018**, *259*, 1004–1010. [[CrossRef](#)]
123. Zhu, Y.; Zhou, W.; Yu, J.; Chen, Y.; Liu, M.; Shao, Z. Enhancing electrocatalytic activity of perovskite oxides by tuning cation deficiency for oxygen reduction and evolution reactions. *Chem. Mater.* **2016**, *28*, 1691–1697. [[CrossRef](#)]
124. Neagu, D.; Tsekouras, G.; Miller, D.N.; Ménard, H.; Irvine, J.T.S. In situ growth of nanoparticles through control of non-stoichiometry. *Nat. Chem.* **2013**, *5*, 916–923. [[CrossRef](#)] [[PubMed](#)]
125. Islam, Q.A.; Majee, R.; Bhattacharyya, S. Bimetallic nanoparticle decorated perovskite oxide for state-of-the-art trifunctional electrocatalysis. *J. Mater. Chem. A* **2019**, *7*, 19453–19464. [[CrossRef](#)]
126. Bloed, C.; Vuong, J.; Enriquez, A.; Raghavan, S.; Tran, I.; Derakhshan, S.; Tavassol, H. Oxygen vacancy and chemical ordering control oxygen evolution activity of  $\text{Sr}_{2-x}\text{Ca}_x\text{Fe}_2\text{O}_{6-\delta}$  Perovskites. *ACS Appl. Energy Mater.* **2019**, *2*, 6140–6145. [[CrossRef](#)]
127. Wang, J.; Gao, Y.; Chen, D.; Liu, J.; Zhang, Z.; Shao, Z.; Ciucci, F. Water splitting with an enhanced bifunctional double perovskite. *ACS Catal.* **2018**, *8*, 364–371. [[CrossRef](#)]
128. Kang, S.M.; Park, S.; Kim, D.; Park, S.Y.; Ruoff, R.S.; Lee, H. Simultaneous reduction and surface functionalization of graphene oxide by mussel-inspired chemistry. *Adv. Funct. Mater.* **2011**, *21*, 108–112. [[CrossRef](#)]
129. Luo, Y.; Wang, K.; Zuo, J.; Qian, Q.; Xu, Y.; Liu, X.; Xue, H.; Chen, Q. Selective corrosion of  $\text{LaCoO}_3$  by NaOH: Structural evolution and enhanced activity for benzene oxidation. *Catal. Sci. Technol.* **2017**, *7*, 496–501. [[CrossRef](#)]
130. Yang, J.; Shi, L.; Li, L.; Fang, Y.; Pan, C.; Zhu, Y.; Liang, Z.; Hoang, S.; Li, Z.; Guo, Y. Surface modification of macroporous  $\text{La}_{0.8}\text{Sr}_{0.2}\text{CoO}_3$  perovskite oxides integrated monolithic catalysts for improved propane oxidation. *Catal. Today* **2021**, *376*, 168–176. [[CrossRef](#)]
131. Yan, S.; Xue, Y.; Li, S.; Shao, G.; Liu, Z. Enhanced bifunctional catalytic activity of manganese oxide/perovskite hierarchical core-shell materials by adjusting the interface for metal-air batteries. *ACS Appl. Mater. Interfaces* **2019**, *11*, 25870–25881. [[CrossRef](#)]
132. Li, W.; Yin, Y.; Xu, K.; Li, F.; Maliutina, K.; Wu, Q.; Li, C.; Zhu, B.; Fan, L. Enhancement of oxygen evolution activity of perovskite  $(\text{La}_{0.8}\text{Sr}_{0.2})_{0.95}\text{MnO}_{3-\delta}$  electrode by Co phase surface modification. *Catal. Today* **2021**, *364*, 148–156. [[CrossRef](#)]

133. Wang, J.; Cheng, X.; Li, Z.; Xu, M.; Lu, Y.; Liu, S.; Zhang, Y.; Sun, C. Perovskite  $\text{Sr}_{0.9}\text{Y}_{0.1}\text{CoO}_{3-\delta}$  nanorods modified with CoO nanoparticles as a bifunctional catalyst for rechargeable Li-O<sub>2</sub> batteries. *ACS Appl. Energy Mater.* **2018**, *1*, 5557–5566. [[CrossRef](#)]
134. Cheng, X.; Kim, B.-J.; Fabbri, E.; Schmidt, T.J. Co/Fe oxyhydroxides supported on perovskite oxides as oxygen evolution reaction catalyst systems. *ACS Appl. Mater. Interfaces* **2019**, *11*, 34787–34795. [[CrossRef](#)] [[PubMed](#)]
135. Zhao, C.; Li, N.; Zhang, R.; Zhu, Z.; Lin, J.; Zhang, K.; Zhao, C. Surface reconstruction of  $\text{La}_{0.8}\text{Sr}_{0.2}\text{Co}_{0.8}\text{Fe}_{0.2}\text{O}_{3-\delta}$  for superimposed OER performance. *ACS Appl. Mater. Interfaces* **2019**, *11*, 47858–47867. [[CrossRef](#)] [[PubMed](#)]
136. Sun, Y.; Li, R.; Chen, X.; Wu, J.; Xie, Y.; Wang, X.; Ma, K.; Wang, L.; Zhang, Z.; Liao, Q.; et al. A-site management prompts the dynamic reconstructed active phase of perovskite oxide OER catalysts. *Adv. Energy Mater.* **2021**, *11*, 2003755. [[CrossRef](#)]
137. Grimaud, A.; Demortière, A.; Saubanère, M.; Dachraoui, W.; Duchamp, M.; Doublet, M.L.; Tarascon, J.M. Activation of surface oxygen sites on an iridium-based model catalyst for the oxygen evolution reaction. *Nat. Energy* **2017**, *2*, 16189. [[CrossRef](#)]
138. Lee, J.G.; Myung, J.H.; Naden, A.B.; Jeon, O.S.; Shul, Y.G.; Irvine, J.T.S. Replacement of Ca by Ni in a perovskite titanate to yield a novel perovskite exsolution architecture for oxygen-evolution reactions. *Adv. Energy Mater.* **2020**, *10*, 1903693. [[CrossRef](#)]
139. Gao, Y.; Lu, Z.; You, T.L.; Wang, J.; Xie, L.; He, J.; Ciucci, F. Energetics of nanoparticle exsolution from perovskite oxides. *J. Phys. Chem. Lett.* **2018**, *9*, 3772–3778. [[CrossRef](#)]
140. Zhang, Y.Q.; Tao, H.B.; Liu, J.; Sun, Y.F.; Chen, J.; Hua, B.; Thundat, T.; Luo, J.L. A rational design for enhanced oxygen reduction: Strongly coupled silver nanoparticles and engineered perovskite nanofibers. *Nano Energy* **2017**, *38*, 392–400. [[CrossRef](#)]
141. Jiang, Y.; Geng, Z.; Yuan, L.; Sun, Y.; Cong, Y.; Huang, K.; Wang, L.; Zhang, W. Nanoscale architecture of  $\text{RuO}_2/\text{La}_{0.9}\text{Fe}_{0.92}\text{Ru}_{0.08-x}\text{O}_{3-\delta}$  composite via manipulating the exsolution of low Ru-substituted A-site deficient perovskite. *ACS Sustain. Chem. Eng.* **2018**, *6*, 11999–12005. [[CrossRef](#)]
142. Zhao, B.; Zhang, L.; Zhen, D.; Yoo, S.; Ding, Y.; Chen, D.; Chen, Y.; Zhang, Q.; Doyle, B.; Xiong, X.; et al. A tailored double perovskite nanofiber catalyst enables ultrafast oxygen evolution. *Nat. Commun.* **2017**, *8*, 14586. [[CrossRef](#)] [[PubMed](#)]
143. Lee, C.; Jeon, Y.; Hata, S.; Park, J.I.; Akiyoshi, R.; Saito, H.; Teraoka, Y.; Shul, Y.G.; Einaga, H. Three-dimensional arrangements of perovskite-type oxide nano-fiber webs for effective soot oxidation. *Appl. Catal. B* **2016**, *191*, 157–164. [[CrossRef](#)]